Received: 6 December 2023 | Revised: 21 June 2024 | Accepted: 11 July 2024

DOI: 10.1002/nme.7574

RESEARCH ARTICLE

WILEY

A condition number-based numerical stabilization method for geometrically nonlinear topology optimization

Lennart Scherz[1] | **Benedikt Kriegesmann**[1] | **Claus B. W. Pedersen**[2]

[1]Institute for Structural Mechanics in Lightweight Design, Hamburg University of Technology, Hamburg, Germany

[2]SIMULIA, Dassault Systemes Deutschland GmbH, Hamburg, Germany

Correspondence
Lennart Scherz, Hamburg Technical University (TUHH), Hamburg, Germany.
Email: Lennart.Scherz@tuhh.de

Abstract

The current paper introduces a new stabilization scheme for void and low-density elements for geometrical nonlinear topology optimization. Frequently, certain localized regions in the geometrical nonlinear finite element analysis of the topology optimization have excessive artificial distortions due to the low stiffness of the void and low-density elements. The present stabilization applies a hyperelastic constitutive material model for the numerical stabilization that is associated with the condition number of the deformation gradient and thereby, is associated with the numerical conditioning of the mapping between current configuration and reference configuration of the underlying continuum mechanics on a constitutive material model level. The stabilization method is independent upon the topology design variables during the optimization iterations. Numerical parametric studies show that the parameters for the constitutive hyperelasticity material of the new stabilization scheme are governed by the stiffness of the constitutive model of the initial physical system. The parametric studies also show that the stabilization scheme is independently upon the type of constitutive model of the physical system and the element types applied for the finite element modeling. The new stabilization scheme is numerical verified using both academic reference examples and industrial applications. The numerical examples show that the number of optimization iterations is significantly reduced compared to the stabilization approaches previously reported in the literature.

KEYWORDS

condition number, geometrically nonlinear modeling, hyperelastic material model, numerical stabilization, static analysis, topology optimization, transient analysis

1 | INTRODUCTION

Numerical instabilities in topology optimization are a prominent issue for geometrically nonlinear modeling using iterative solvers. The numerical instabilities arise from an ill-conditioned global stiffness operator. This causes convergence problems in the iterative solver for the primal solution and thereby, often the analysis fails. Especially density-based

Int J Numer Methods Eng. 2024;125:e7574.
https://doi.org/10.1002/nme.7574

topology optimizations including geometric non-linearities are subject to these instabilities, since they incorporate high stiffness ratios in the order of 10^6 to 10^9 between solid and void elements. Thereby, the void and intermediate density elements can exhibit localized artificial buckling. Various approaches to stabilize this phenomenon are found in literature which are briefly discussed in the following. These are also categorized in Figure 1.

Overall stiffness increase[1,2] This is the most trivial approach for which the lower bound on the elemental stiffness is increased. This prevents numerical instabilities, but it also changes the underlying physical system behavior, if the ratio between solid and void stiffness is larger than 10^6.[3] Therefore, this approach is not feasible if physical accuracy is required.

Element removal[3–6] This approach removes or reintroduces elements depending on a certain lower density threshold. Thereby, low-density elements that would cause numerical instabilities are excluded from the analysis. The element removal and element reintroduction is often based on heuristic parameters and generally needs many optimization iterations to converge. Another drawback is that this approach is indiscriminatory with respect to whether or not a low-density element will cause numerical instabilities or not during the calculation of the primal solution.

Fictitious domain[7–10] This approach interpolates the elemental geometrically linear and nonlinear stiffness operator of a system. The solid regions in a topology design are modeled as geometrically nonlinear while the void regions are modeled as geometrically linear. Intermediate densities are interpolated between the two cases by a Heaviside function. Modeling void elements as geometrically linear avoids numerical instabilities arising from geometrically nonlinear effects. A drawback of this approach is that the geometrically linear stiffness operators changes the physical system behavior of the elements. Especially for the stiffness of the intermediate density elements and over the optimization iterations this can have a significant effect. Therefore, the interpolation parameters have to be changed incrementally for very large deformations, which causes many optimization iterations and high computational cost.

Relaxed convergence criteria[11–13] This approach does not prevent the numerical instabilities of the intermediate and void elements. Instead, it excludes degrees of freedom that are surrounded by void elements from the convergence check of the iterative solver scheme. A drawback of this approach is that the excluded degrees of freedom often show

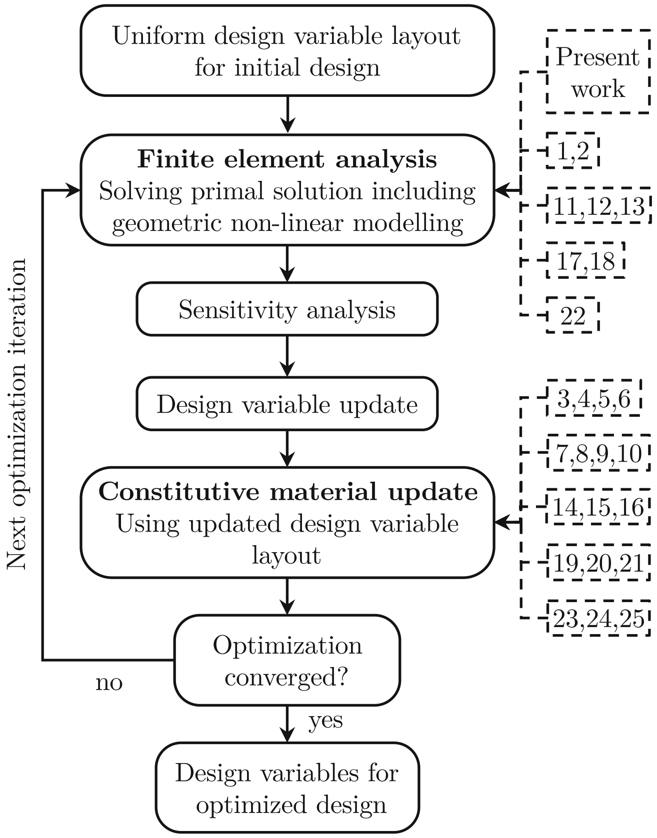

FIGURE 1 Reference overview of stabilization schemes addressing numerical instabilities arising from geometrically nonlinear modeling and where these schemes are incorporated in the optimization workflow.

oscillatory behavior when solving for the primal solution, causing many solver iterations or even divergence of the primal solution.

Hyperelastic base material[14–16] This approach applies a hyperelastic formulation for the base material of the topology optimization. This type of constitutive modeling is often numerically more stable for larger strains, but this still does not guarantee that no numerical instabilities are present. Another drawback of this approach is that it can only be applied to specific materials like rubber, which can be modeled using a hyperelastic constitutive material model.

Third medium approach[10,17,18] This approach applies a hyperelastic base material to model internal contact during the topology optimization. It adds a void regularization term to the hyperelastic strain energy potential of the material to stabilize the low-density elements. The void regularization term is based on the Hessian of the displacement field as well as a linear scaling factor, which penalizes higher order deformation modes. Additionally, the penalization is interpolated according to the element density using a Heaviside function. This is the most similar to the approach of the present work, although it significantly differs in its hyperelastic penalization term using the Hessian of the displacement field as well as its incorporation into the constitutive modeling, which is limited to hyperelastic material models. Furthermore, the Hessian introduces a dimension dependence into the regularization term, which has to be compensated by a characteristic length factor.

Plastic material interpolation[19–21] This scheme applies different penalization parameters for the plastic yielding and/or hardening than the penalization parameter for the elastic Young's modulus to suppress numerical instabilities that occur in models considering both elastoplastic material behavior and geometrically nonlinear modeling. A drawback of this approach are discontinuous sensitivities at the yield point as shown in Reference 21. Also, this approach is only applicable for suppressing the numerical instabilities that arise due to the elastoplastic yielding behavior in geometrically nonlinear modeling.

Levenberg–Marquardt algorithm[22] This approach applies an iterative solver scheme that is more robust with respect to an ill-conditioned stiffness operator. Drawbacks of this approach are that the parameters for this scheme are non-trivial and this approach still does not ensure convergence of the iterative scheme for the primal solution. Furthermore, it is numerically more expensive than the usual numerical solver schemes for the primal solution.

Element connectivity parameterization[23–25] Instead of a density-based topology optimization approach, this approach optimizes the connections between elements modeled as spring stiffnesses. Hence, no high ratios between elemental stiffnesses are included in the modeling, thereby no numerical instabilities are present. A drawback of this approach is that the optimized designs cannot directly be transformed into manufacturable designs. Furthermore, the parameters applied for the spring stiffnesses and the optimization are non-trivial as the physical accuracy of the results is not guaranteed.

1.1 | Present work and approach

The present work applies a constitutive hyperelastic strain energy potential to penalize numerically ill-conditioned void and intermediate density elements. In that aspect it is similar to the third-medium approach, but has the following fundamental differences and enhancements:

- The stabilization strain energy potential incorporates the numerical condition number of the deformation gradient expressed in terms of its invariants and thereby, penalizes element configurations in which the isoparametric element mapping is close to being singular at the material points.
- The stabilization is superimposed with the physical system by applying an element duplication scheme and therefore, is not limited to physical systems having hyperelastic constitutive modeling.
- The stabilization strain energy potential is independent of the design variable values during the topology optimization.
- The parameters for the stabilization only depend on the stiffness of the base material for the physical system and is independent of the element type.

Therefore, the approach in the present work is only applied during the finite element analysis for the topology optimization workflow. Additionally, the approach can also be generalized to stabilize numerically unstable finite element analyses independent of if it is conducted as part of a topology optimization or not.

2 | METHODS

This section provides a brief overview for the applied finite strain theory, numerical conditioning of mathematical problems as well as the applied topology optimization formulation. Afterwards, these are applied in the novel stabilization scheme presented in this work.

2.1 | Finite strain theory

This part provides an overview over the measures for the finite strain theory defined in Reference 26 that are required for the present approach.

The deformation gradient relates an infinitesimal change ∂x in the deformed configuration to an infinitesimal change ∂X in the undeformed configuration as shown in Figure 2 and is defined as

$$\boldsymbol{F} = \frac{\partial x}{\partial X}. \tag{1}$$

The change in volume between the current and the reference configuration is defined by

$$J = \det(\boldsymbol{F}). \tag{2}$$

The volumetric change in the deformation gradient $\boldsymbol{F}$ can be eliminated by

$$\overline{\boldsymbol{F}} = J^{-\frac{1}{3}}\boldsymbol{F}, \tag{3}$$

allowing to separate the deviatoric deformation state from the volumetric deformation state for constitutive modeling. The deformation gradient is multiplied with its transpose to eliminate its rotational part and thereby, only the part causing the deformation between the two configurations is modeled. This yields either the right Cauchy–Green deformation tensor

$$\boldsymbol{C} = \boldsymbol{F}^T\boldsymbol{F}. \tag{4}$$

or left Cauchy–Green deformation tensor

$$\boldsymbol{B} = \boldsymbol{F}\boldsymbol{F}^T. \tag{5}$$

depending on if a total Lagrangian or an updated Lagrangian formulation is applied. In this work we applied, the left Cauchy–Green deformation tensor. The volumetric change can be again eliminated from $\boldsymbol{B}$ by

$$\overline{\boldsymbol{B}} = \overline{\boldsymbol{F}}\,\overline{\boldsymbol{F}}^T. \tag{6}$$

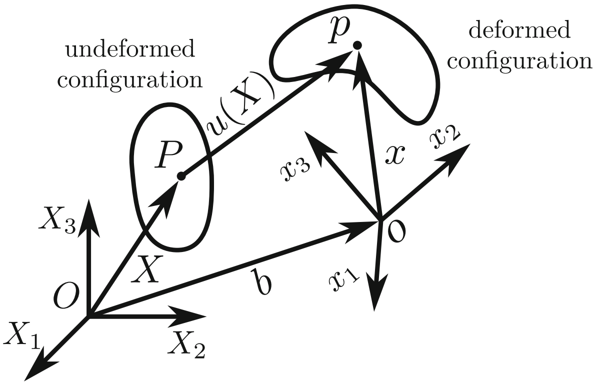

FIGURE 2 Material point nomenclature for the undeformed and deformed configuration in finite strain theory.

The eigenvalues of $\boldsymbol{B}$ and $\overline{\boldsymbol{B}}$ are the squared principle stretches and squared deviatoric principle stretches respectively

$$\mathrm{eig}(\boldsymbol{B}) = \{\lambda_1^2, \lambda_2^2, \lambda_3^2\}, \tag{7}$$

$$\mathrm{eig}(\overline{\boldsymbol{B}}) = \{\overline{\lambda}_1^2, \overline{\lambda}_2^2, \overline{\lambda}_3^2\}, \tag{8}$$

which are the squared singular values of $\boldsymbol{F}$ and $\overline{\boldsymbol{F}}$ respectively. They can be converted into each other by

$$\overline{\lambda_i} = J^{-\frac{1}{3}}\lambda_i. \tag{9}$$

The matrix invariants of $\overline{\boldsymbol{B}}$ together with J are often applied to define a hyperelastic constitutive material laws, since they are invariant with respect to rotation. The invariants applied in this work are defined as

$$\overline{I}_1 = \overline{\lambda}_1^2 + \overline{\lambda}_2^2 + \overline{\lambda}_3^2, \tag{10}$$

$$\overline{I}_2 = \frac{1}{\overline{\lambda}_1^2} + \frac{1}{\overline{\lambda}_2^2} + \frac{1}{\overline{\lambda}_3^2}, \tag{11}$$

$$J = \lambda_1\lambda_2\lambda_3. \tag{12}$$

The deformation gradient can also be expressed in terms of the derivatives of the shape functions in isoparametric finite element formulations as

$$\boldsymbol{F} = \left(\sum_{i=1}^{n_{\text{nodes}}} \frac{\partial h_i(\boldsymbol{\xi})}{\partial \boldsymbol{\xi}} \boldsymbol{x}_i\right)\left(\sum_{i=1}^{n_{\text{nodes}}} \frac{\partial h_i(\boldsymbol{\xi})}{\partial \boldsymbol{\xi}} \boldsymbol{X}_i\right)^{-1}, \tag{13}$$

where n_{nodes} are the number of nodes, $\boldsymbol{\xi}$ are the natural coordinates of the isoparametric elements and $\boldsymbol{x}_i$ and $\boldsymbol{X}_i$ are the nodal coordinates in the current as well as the reference configuration.

2.1.1 | Strain measures

There are various finite strain measures applied for constitutive modeling. The Green-Lagrange strain tensor $\boldsymbol{\varepsilon}_G$ and the Almansi strain tensor $\boldsymbol{\varepsilon}_A$ are defied as

$$\boldsymbol{\varepsilon}_G = \frac{1}{2}(\boldsymbol{C} - \boldsymbol{I}), \tag{14}$$

$$\boldsymbol{\varepsilon}_A = \frac{1}{2}(\boldsymbol{I} - \boldsymbol{B}), \tag{15}$$

and are often applied for modeling hyperelastic behavior of rubber-like materials. For elastoplasticity, the logarithmic or Hencky strain tensor

$$\boldsymbol{\varepsilon}_H = \ln\left(\sqrt{\boldsymbol{F}\boldsymbol{F}^T}\right) \tag{16}$$

is often applied. All strain measures in the present work for the physical system modeling are expressed in term of the Hencky strain.

2.1.2 | Constitutive modeling

In the present paper, we apply purely linear elastic, elastoplastic as well as hyperelastic constitutive modeling. The linear elasticity is modeled by the linear relationship

$$\boldsymbol{\sigma} = \boldsymbol{D}^{\text{el}} : \boldsymbol{\varepsilon}_H, \tag{17}$$

where $\boldsymbol{\sigma}$ is the Cauchy-stress tensor, $\boldsymbol{D}^{\mathrm{el}}$ is the forth order elastic tensor and $\boldsymbol{\varepsilon}_H$ is the logarithmic or Hencky strain tensor. $\boldsymbol{D}^{\mathrm{el}}$ is a function of the Young's modulus E and the Poisson ratio ν. This is also the same constitutive relationship applied for the elastic response in the elastoplastic constitutive modeling. The elastoplasticity is modeled by dividing the deformation gradient into an elastic and a plastic part

$$\boldsymbol{F} = \boldsymbol{F}^{\mathrm{el}} \cdot \boldsymbol{F}^{\mathrm{pl}}. \tag{18}$$

This decomposition is calculated by integrating the total strain rate

$$\dot{\boldsymbol{\varepsilon}} = \dot{\boldsymbol{\varepsilon}}^{\mathrm{el}} + \dot{\boldsymbol{\varepsilon}}^{\mathrm{pl}} \tag{19}$$

over time, where $\dot{\boldsymbol{\varepsilon}}^{\mathrm{el}}$ is the elastic strain rate and $\dot{\boldsymbol{\varepsilon}}^{\mathrm{pl}}$ the plastic strain rate. The plastic strain rate are governed by a yield function, while the elastic strain rate is derived from $\boldsymbol{F}^{\mathrm{el}}$ using a hyperelastic strain energy potential. We applied a Mieses yield criterion using the Cauchy stresses in combination with isotropic hardening for the elastoplastic examples in this article. These strain rates have to be solved iteratively to satisfy the yield function for each strain increment. Note, that this integration of the strain rate is also applied for the purely elastic constitutive modeling. Hence, the linear elastic constitutive modeling is not directly derived from a strain energy potential. The hyperelastic modeling in this article applies an invariant-based hyperelastic strain energy potential

$$U = U(\bar{I}_1, \bar{I}_2, J), \tag{20}$$

and is hence based on the invariants of the left Cauchy–Green deformation tensor $\boldsymbol{B}$.

2.2 | Numerical condition number of a matrix

The condition number of a problem $\mathcal{P} : \mathbb{R}^n \rightarrow \mathbb{R}^m$ describes the relationship between an error in the input of the problem $\mathcal{P}$ and the resulting error in the output of $\mathcal{P}$. Let the component-wise relative input error be bound by

$$\frac{|\hat{x}_i - x_i|}{|x_i|} \leq \epsilon \qquad x_i \in \boldsymbol{x}, \hat{x}_i \in \hat{\boldsymbol{x}}, \tag{21}$$

where $\boldsymbol{x}$ is the unperturbed and $\hat{\boldsymbol{x}}$ the perturbed input. The condition number κ of $\mathcal{P}$ then bounds the relative output error as follows:

$$\frac{||\mathcal{P}(\hat{\boldsymbol{x}}) - \mathcal{P}(\boldsymbol{x})||}{||\mathcal{P}(\boldsymbol{x})||} \leq \kappa\epsilon + \mathcal{O}(\epsilon). \tag{22}$$

In the following, the condition number of matrices are further discussed. A condition number of a matrix $\boldsymbol{A} \in \mathbb{R}^{m\times n}$ describes the impact an error of a perturbed input $x + \varepsilon$ has on solving the linear system $\boldsymbol{A}(x + \varepsilon) = b$ and therefore, how close the matrix $\boldsymbol{A}$ is to being singular. In case $\boldsymbol{A}$ is non-singular, its condition number is defined as

$$\kappa(\boldsymbol{A}) := ||\boldsymbol{A}|| \cdot ||\boldsymbol{A}^{-1}|| \tag{23}$$

with respect to a consistent matrix norm $|| \cdot ||$. The condition number induced by the Frobenius norm $|| \cdot ||_F$ is applied in the present work. The Frobenius norm is defined as

$$|| \cdot ||_F = \left(\sum_{i=1}^{m} \sum_{j=1}^{n} |a_{ij}|^2 \right)^{\frac{1}{2}} = \sqrt{\operatorname{tr}(\boldsymbol{A}^* \boldsymbol{A})}, \tag{24}$$

where $\operatorname{tr}(\boldsymbol{A}^*\boldsymbol{A})$ is the trace of $\boldsymbol{A}^*\boldsymbol{A}$. In case that $\boldsymbol{A}$ is a regular square matrix, the trace can be expressed in terms of the eigenvalues λ_i of $\boldsymbol{A}$, yielding

$$|| \cdot ||_F = \sqrt{\sum \lambda_i^2(\boldsymbol{A})}. \tag{25}$$

The condition number induced by the Frobenius norm then yields

$$\kappa_F(\boldsymbol{A}) = \sqrt{\mathrm{tr}(\boldsymbol{A}^*\boldsymbol{A})} \cdot \sqrt{\mathrm{tr}(\boldsymbol{A}^{-*}\boldsymbol{A}^{-1})} = \sqrt{\sum \mathrm{eig}(\boldsymbol{A}^*\boldsymbol{A})} \cdot \sqrt{\sum \frac{1}{\mathrm{eig}(\boldsymbol{A}^*\boldsymbol{A})}}. \tag{26}$$

The condition of a matrix A number induced by a different norm can be bound by applying the equivalence of norms. For example, the $\| \cdot \|_2$ norm is bound by

$$\frac{1}{\sqrt{\min(m,n)}} \|\boldsymbol{A}\|_F \le \|\boldsymbol{A}\|_2 \le \|\boldsymbol{A}\|_F, \tag{27}$$

and thereby, the condition number $\kappa_2(\boldsymbol{A})$ is bound by

$$\frac{1}{\min(m,n)} \cdot \kappa_f(\boldsymbol{A}) \le \kappa_2(\boldsymbol{A}) \le \kappa_F(\boldsymbol{A}). \tag{28}$$

Hence, the condition number induced by the Frobenius norm is equivalent to any other condition number induced by any other norm and their difference is bound by constants.

2.3 | Topology optimization formulation

This work applies a density based topology optimization approach, in which the material properties like the elastic Young's modulus and elastoplastic material parameters for yielding and hardening are interpolated using the SIMP approach (see Reference 2). The plastic material parameters for the elastoplastic constitutive modeling are interpolated using the same penalization as the elastic material parameters resulting in the stress-strain-curves shown in Figure 3 having a constant yield strain independent of the design variable as described in Reference 21. Design variable filtering is applied in this article to regularize the density based topology optimization problem and ensure mesh independency as well as prevent checker boarding as described in Reference 4. No continuation schemes or projection methods are applied in this work. All optimizations in this work are conducted in Simulia Tosca Structure[27] and apply Simulia Abaqus[28] as finite element solver. However, the present approach can be applied for all finite element solvers allowing geometrically nonlinear modeling and strain energy potential based constitutive material modeling.

Two stopping criteria are applied which evaluate the change in density and change in objective value between the optimization iterations as shown in Figure 1:

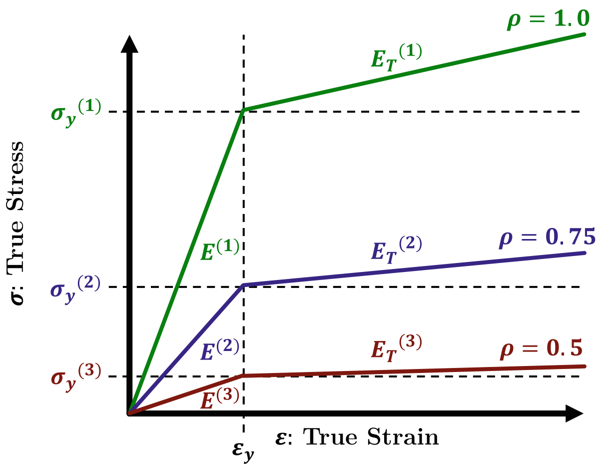

FIGURE 3 Material interpolation applied for plastic constitutive modeling having a penalization where the yield strain is independent of the design variables.

- Average change in density ρ:

$$\frac{\sum_{m=1}^{M} |\rho_{i,n} - \rho_{i,n-1}|}{M} \leq \Delta\rho_{\text{ave, stop}}, \tag{29}$$

where M is the number of elements in the design space.

- Relative change in objective function value Θ:

$$\frac{|\Theta_n - \Theta_{n-1}|}{|\Theta_n|} \leq \Delta\Theta_{\text{stop}}, \tag{30}$$

where the stopping criteria applied in the present work are set to $\Delta\rho_{\text{ave, stop}} = 0.005$ and $\Delta\Theta_{\text{stop}} = 0.001$.

2.4 | Stabilization scheme

The present stabilization scheme applies an artificial constitutive material law that penalizes ill-conditioning terms at the constitutive material point level. This artificial behavior is then superimposed with the physical behavior of the system as shown in Figure 4. The artificial constitutive material law incorporates the squared condition number κ_F of the deformation gradient $\boldsymbol{F}$ as a hyperelastic strain energy potential. Thereby, the stresses induced by the hyperelastic strain energy potential material law are equivalent to the derivative of the condition number at that material point. Hence, this material law induces stresses which improve the condition number at the material points in case an element moves towards a configuration in which a material point is ill-conditioned. The condition number of $\boldsymbol{F}$ is also related to the condition number of the right and left Cauchy–Green deformation Tensors $\boldsymbol{C}$ and $\boldsymbol{B}$. When considering Equation (13) the condition number of $\boldsymbol{F}$ can be interpreted as the numerical conditioning of the isoparametric mapping from the current to the natural coordinate system. An ill-conditioning or singularity in this mapping causes an ill-conditioning of all measures for geometrically nonlinear analysis. In the following, a novel proof linking the condition number of the deformation gradient to the first and second invariants of the left Cauchy–Green deformation tensor $\boldsymbol{B}$ is derived in Section 2.4.1, yielding the relationship

$$\kappa_F^2(\boldsymbol{F}) = I_1 I_2 = \bar{I}_1 \bar{I}_2 \geq \kappa_F(\boldsymbol{B}) = \kappa_F(\boldsymbol{C}). \tag{31}$$

This relationship in (31) is then applied to formulate the artificial strain energy potential for the stabilization scheme. Unlike the regularization terms in References 10,17, and 18 applying the Hessian of the deformation gradient,

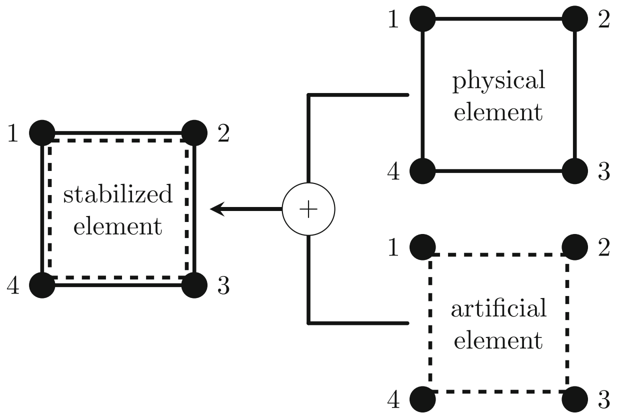

FIGURE 4 Element superposition scheme applying a hyperelastic constitutive model for numerical stabilization (artificial element) into a physical finite element model (physical element) using a numerically non-intrusive approach. The two elements share the same nodes, but differ in their constitutive modeling.

the Equation (31) is independent of the model dimensions and therefore, does not require a characteristic length factor.

2.4.1 | Proof

The condition number of the deformation gradient $\boldsymbol{F}$ induced by the Frobenius norm in (23) yields

$$\kappa_F(\boldsymbol{F}) = \|\boldsymbol{F}\|_F \cdot \|\boldsymbol{F}^{-1}\|_F. \tag{32}$$

These Frobenius norms can be expressed as the square roots of the traces of $\boldsymbol{F}^T\boldsymbol{F}$ and $\boldsymbol{F}^{-T}\boldsymbol{F}^{-1}$, where $(\dots)^{-T} := \left((\dots)^T\right)^{-1} = \left((\dots)^{-1}\right)^T$ as shown i n (26), yielding

$$\kappa_F(\boldsymbol{F}) = \sqrt{\operatorname{tr}\left(\boldsymbol{F}^T\boldsymbol{F}\right)} \cdot \sqrt{\operatorname{tr}\left(\boldsymbol{F}^{-T}\boldsymbol{F}^{-1}\right)}. \tag{33}$$

For the trace of a matrix product of two square matrices $\boldsymbol{A}_1, \boldsymbol{A}_2$ it holds that $\operatorname{tr}(\boldsymbol{A}_1\boldsymbol{A}_2) = \operatorname{tr}(\boldsymbol{A}_2\boldsymbol{A}_1)$. Therefore, the first term in (33) can be rewritten as

$$\kappa_F(\boldsymbol{F}) = \sqrt{\operatorname{tr}\left(\boldsymbol{F}\boldsymbol{F}^T\right)} \cdot \sqrt{\operatorname{tr}\left(\boldsymbol{F}^{-T}\boldsymbol{F}^{-1}\right)}. \tag{34}$$

Since for two invertible matrices $\boldsymbol{A}_1, \boldsymbol{A}_2 \in \mathbb{R}^{n\times n}$ it holds that $\boldsymbol{A}_1^{-1}\boldsymbol{A}_2^{-1} = (\boldsymbol{A}_2\boldsymbol{A}_1)^{-1}$, the last term can be rewritten as

$$\kappa_F(\boldsymbol{F}) = \sqrt{\operatorname{tr}\left(\boldsymbol{F}\boldsymbol{F}^T\right)} \cdot \sqrt{\operatorname{tr}\left(\left(\boldsymbol{F}\boldsymbol{F}^T\right)^{-1}\right)}. \tag{35}$$

Using the definition of the left Cauchy–Green deformation tensor (5) this expression yields

$$\kappa_F(\boldsymbol{F}) = \sqrt{\operatorname{tr}(\boldsymbol{B})} \cdot \sqrt{\operatorname{tr}\left(\boldsymbol{B}^{-1}\right)}. \tag{36}$$

The trace of a regular square matrix $\boldsymbol{A} \in \mathbb{R}^{n\times n}$ can be expressed as the sum of its eigenvalues

$$\operatorname{tr}(\boldsymbol{A}) = \sum_{i=1}^{n} \operatorname{eig}(\boldsymbol{A})_i. \tag{37}$$

Furthermore, the relationship between the eigenvalues of a invertible matrix $\boldsymbol{A}$ and its inverse $\boldsymbol{A}^{-1}$ is

$$\operatorname{eig}(\boldsymbol{A}^{-1})_i = \frac{1}{\operatorname{eig}(\boldsymbol{A})_i}, \tag{38}$$

which is trivial, when considering the eigen decomposition of these two matrices. Applying (37) and (38) to (36) yields

$$\kappa_F(\boldsymbol{F}) = \sqrt{\sum_{i=1}^{3} \operatorname{eig}(\boldsymbol{B})} \cdot \sqrt{\sum_{i=1}^{3} \frac{1}{\operatorname{eig}(\boldsymbol{B})}}. \tag{39}$$

Substituting the definition of the principle stretches (7) into (39) yields

$$\kappa_F(\boldsymbol{F}) = \sqrt{\lambda_1^2 + \lambda_2^2 + \lambda_3^2} \cdot \sqrt{\frac{1}{\lambda_1^2} + \frac{1}{\lambda_2^2} + \frac{1}{\lambda_3^2}}. \tag{40}$$

Rearranging the definition of the deviatoric principle stretches (8) for the principle stretches yields

$$\overline{\lambda_i} = (\lambda_1\lambda_2\lambda_3)^{-\frac{1}{3}}\lambda_i \Rightarrow \lambda_i = (\lambda_1\lambda_2\lambda_3)^{\frac{1}{3}}\overline{\lambda_i}. \tag{41}$$

Substituting (41) into (40) yields

$$\kappa_F(\boldsymbol{F}) = \sqrt{\overline{\lambda}_1^{-2} + \overline{\lambda}_2^{-2} + \overline{\lambda}_3^{-2}} \cdot \sqrt{\frac{1}{\overline{\lambda}_1^{-2}} + \frac{1}{\overline{\lambda}_2^{-2}} + \frac{1}{\overline{\lambda}_3^{-2}}}. \tag{42}$$

Note, that the $(\lambda_1\lambda_2\lambda_3)^{\frac{1}{3}}$ terms for both roots cancel each other. Next, the definitions in (10) and (11) for the first and second invariants $\overline{I}_1$ and $\overline{I}_2$ are substituted into (42), finally yielding

$$\kappa_F(\boldsymbol{F}) = \sqrt{\overline{I}_1} \cdot \sqrt{\overline{I}_2} = \sqrt{\overline{I}_1\overline{I}_2} \Rightarrow \kappa_F^2(\boldsymbol{F}) = \overline{I}_1 \cdot \overline{I}_2, \tag{43}$$

which completes the first part of the proof. For the second part of the proof, we apply the relationship for the condition number of a matrix product. Let $\boldsymbol{A}_1$ and $\boldsymbol{A}_2$ be two invertible matrices $\boldsymbol{A}_1, \boldsymbol{A}_2 \in \mathbb{R}^{n\times n}$, then it holds that

$$\kappa(\boldsymbol{A}_1\boldsymbol{A}_2) \leq \kappa(\boldsymbol{A}_1)\kappa(\boldsymbol{A}_2). \tag{44}$$

Therefore, the condition number of the left Cauchy–Green deformation tensor $\boldsymbol{B}$ can be approximated as

$$\kappa_F(\boldsymbol{B}) \leq \kappa_F(\boldsymbol{F})\kappa_F(\boldsymbol{F}^T) = \kappa_F^2(\boldsymbol{F}) = \overline{I}_1 \cdot \overline{I}_2. \tag{45}$$

Lastly, it can be shown that $\kappa_F(\boldsymbol{B}) = \kappa_F(\boldsymbol{C})$, which is trivial to show, since the Frobenius norm of two square matrices $\|\boldsymbol{A}_1\boldsymbol{A}_2\|_F = \|\boldsymbol{A}_2\boldsymbol{A}_1\|_F$. Therefore, the same proof is applicable for the right Cauchy–Green deformation tensor $\boldsymbol{C}$.

Note, that (40) can be simplified in a similar fashion using the principle stretches λ_i instead of the deviatoric stretches $\overline{\lambda}_i$ and that $\overline{I}_1\overline{I}_2 = I_1I_2$. This shows an important observation that the condition numbers of $\boldsymbol{F}$ and $\boldsymbol{C}$ are not dependent on the volumetric stretches. Thereby, they do not influence the numerical conditioning on a constitutive material model level. Nonetheless, excessive volumetric compression or tension can lead to convergence issues due to rounding errors in the nodal coordinates of the finite element method. Furthermore, this also does not prevent locking phenomena due to the finite element discretization from occurring.

2.4.2 | Numerical implementation

A strain energy potential incorporating the condition number $\kappa_F^2(\boldsymbol{C})$ is implemented using a specific combination of parameters for the compressible polynomial hyperelastic strain energy potential[29] formula is defined as

$$U := \sum_{\substack{i,j=0\\ i+j\neq 0\\ i+j\leq N}}^{N} C_{ij}\left(\overline{I}_1 - 3\right)^i\left(\overline{I}_2 - 3\right)^j + \sum_{i=1}^{N}\frac{1}{D_i}\left((J^{\mathrm{el}}) - 1\right)^{2i}. \tag{46}$$

The material parameter nomenclature in Equation (46) is in correspondence with the Abaqus implementation.[28] The term $(\overline{I}_1\overline{I}_2 - 9)$ can be isolated from (46) by applying the coefficients shown in Table 1. The polynomial coefficients yielding higher order terms of $\kappa_F^2(\boldsymbol{F})$ are shown in appendix Table A1.

Additionally, a volumetric part is added to the strain energy potential to prevent excessive volumetric compression. Otherwise this material law penalizes further deviatoric deformation of ill-conditioned elements and thereby, transforms

TABLE 1 Coefficients for a polynomial hyperelastic strain energy potential for which the condition number-based term $(\overline{I}_1\overline{I}_2 - 9)$ is isolated.

C_{10}	C_{01}	C_{11}	C_{20}	C_{02}
3	3	1	0	0

the energy into volumetric deformation. Therefore, the artificial strain energy potential applied in this article yields

$$U := C_\kappa \cdot (\overline{I}_1\overline{I}_2 - 9) + \frac{1}{D_2} \cdot \left(J^{\mathrm{el}} - 1\right)^4, \tag{47}$$

where C_κ and D_2 are model parameters for the numerical stabilization. These are related to the physical element material parameters, as discussed in the following section. Note, that the volumetric parameter D_2 is not related to the condition of the deformation gradient and is only included to avoid excessive volumetric compression or tension. Due to the implementation of the strain energy potential in (46) in Abaqus the parameter D_1 cannot be omitted in the element definition. Therefore, D_1 is set to $10^9 \cdot D_2$ to avoid an error message, while having numerically no influence on the constitutive modeling. A workflow is developed to implement the present stabilization scheme into an arbitrary finite element model using the numerically non-intrusive approach as discussed in 2.4. The elements inside the design space to be stabilized are duplicated and then assigned a hyperelastic constitutive material law that includes the condition number-based measure $\overline{I}_1\overline{I}_2$ as its strain energy potential. Thereby, the stabilization scheme can be applied to any arbitrary finite element model as long as a hyperelastic finite strain formulation is numerically supported by the finite element solver. Therefore, the present approach is not limited to topology optimization application and is generally applicable to all geometrically nonlinear finite element models requiring numerical stabilization.

3 | NUMERICAL RESULTS

The first part of this section focuses on a parametric study to calibrate suitable stabilization model parameters. The second part then applies the calibrated stabilization model to both academic and industrial topology optimization applications.

3.1 | Parametric study and stabilization material model calibration using a C-shaped structure

A well-known example from Reference 7 shown in Figure 5 is applied to calibrate the hyperelastic parameters for the stabilization scheme.

The model consists of a C-shaped solid structure having the dimensions $10 \times 10 \times 1$. The structure is loaded vertically at its upper beam and horizontally at the lower beam. The structure is modeled in two different ways: once by considering only the physical structure (5a), in the following referenced as solid-only version, and once by additional modeling an artificial void region, which is encapsulated in the structure (5b), in the following referenced as solid-void version. The solid-only version serves as a reference solution of the system, while the solid-void version represents a model that is prone to numerical instabilities arising due to geometric nonlinear modeling. The materials are modeled using a linear elastic constitutive material law. The solid region applies a Young's modulus of $E = 1$ and a Poisson's ratio of $\nu = 0.3$. The artificial void region applies the same material law but with a significantly lower Young's modulus of $E = 10^{-9}$. Furthermore, a thicker 3D version of this model (Figure 5C,D) having the dimensions $10 \times 10 \times 10$ is investigated to extend the scope of this parametric study to also include 3D element types. The forces F_1 and F_2 are applied to each node of the corresponding edge. Furthermore, the forces are scaled such that their respective sum is equivalent to 10 times the force acting in the 2D case to account for the increase in the structures thickness. The structures are discretized by applying the different element types as shown in Table 2

3.1.1 | Parametric study setup

For the parametric study, the novel stabilization scheme is applied to stabilize the solid-void versions of the 2D- and 3D-model. All elements in the models are duplicated and assigned the same hyperelastic stabilization material model defined in (47). The 2D model is investigated using linear and quadratic triangular elements (CPS3 & CPS6) as well as linear fully-integrated and reduced quadrilateral elements (CPS4 & CPS4R). The 3D model is investigated using linear and quadratic tetrahedral elements (C3D4 & C3D10) as well as linear fully integrated and reduced hexagonal elements

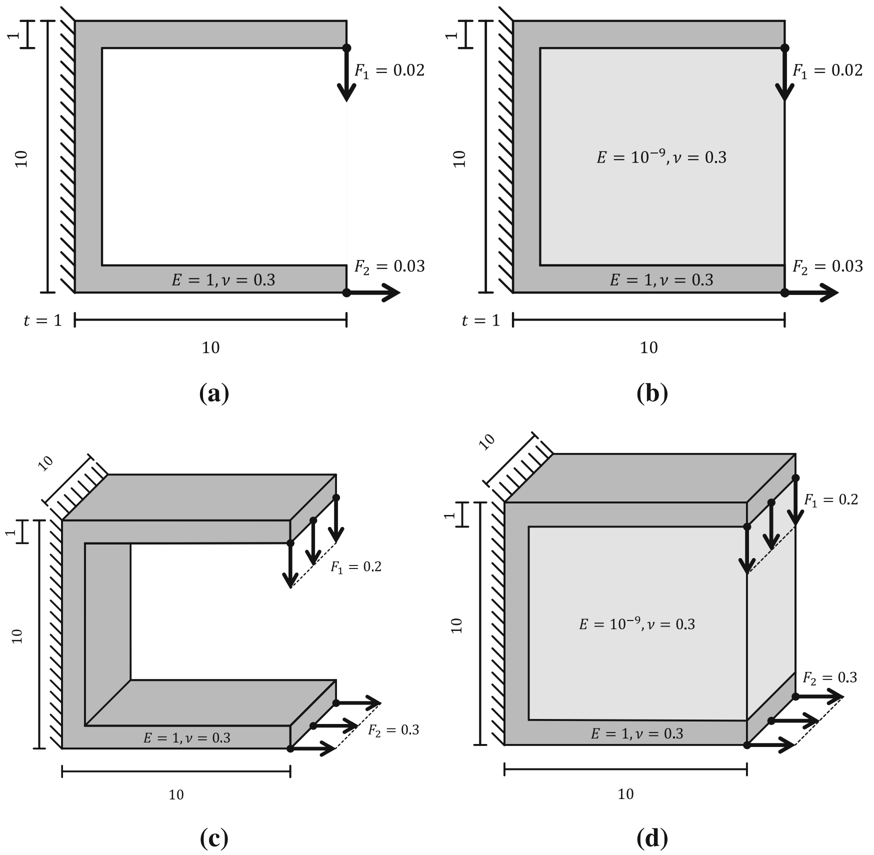

FIGURE 5 C-shaped solid-void structure modeled as (A) 2D elements without void elements (B) 2D elements including void elements (C) 3D elements without void elements (D) 3D elements including void elements. Note that the 3D structure is 10 times thicker than the 2D structure and the acting forces are scaled accordingly.

TABLE 2 Solid-void model discretizations for the different element types.

	CPS3 & CPS6	CPS4 & CPS4R	C3D4 & C3D10	C3D8 & C3D8R
Solid-only	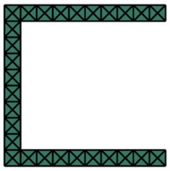	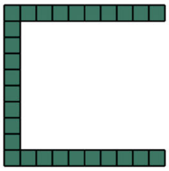	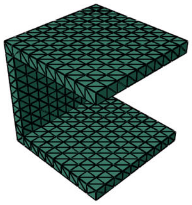	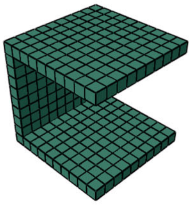
Solid-void	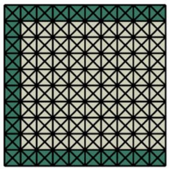	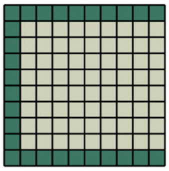	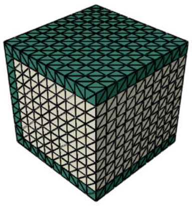	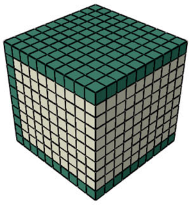

(C3D8 & C3D8R). The material parameter combinations $C_\kappa \times D_2$ are investigated for

$$C_\kappa = 10^{\{-13;-12.5,\dots;0.5;0\}}, \tag{48}$$

$$\frac{1}{D_2} = 10^{\{-13;-12.5,\dots;0.5;0\}}, \tag{49}$$

yielding 729 combinations per element type and 5832 in total for the parametric study. The reciprocal scaling of D_2 is required due to its definition in the polynomial form hyperelastic strain energy potential in polynomial form in (46).

3.1.2 | Parametric study evaluation measures

The results of the parametric study are evaluated in terms of numerical stability and physical accuracy. For this purpose, the following three dimensionless evaluation measures are defined:

- t_comp: Relative completed analysis time.
- u_comp: Relative completed nodal displacement.
- u_error: Relative time-adjusted nodal displacement error.

The first two measures describe how much of the load application and deformation state was achieved before divergence occurred. The last measure describes the difference between the stabilized solid-void model and the reference solid-only model. In the following, the calculations of the three measures are explained in more detail.

Relative completed time The completed time measure is calculated as

$$t_\text{comp} = \frac{t_\text{last}}{t_\text{ref}}, \tag{50}$$

where t_ref is the full analysis time of the reference analysis. t_last is the last time point during the analysis for which the Newton–Raphson scheme achieved convergence. In case of a converged analysis $t_\text{last} = t_\text{ref}$. Since the loading for this model is applied in a time-wise linear manner, this measure is also equivalent to the relative completed loading.

Relative completed nodal displacement The nodal displacements of the two loading points in the solid-void analyses evaluated at t_last are normalized with their corresponding values from the reference solution evaluated at t_ref. Their absolute values are then combined in a weighted sum, yielding

$$u_\text{comp} := \sum_i w_i \cdot \frac{|u_i|}{|u_{i,\text{ref}}|} \qquad \text{for} \quad i = \{\dots_{1,F_1}, \dots_{2,F_1}, \dots_{1,F_2}, \dots_{2,F_2}\}. \tag{51}$$

The weights w_i are chosen as the relative values of the nodal displacements at the end of the reference solution, yielding

$$w_i := \frac{|u_{i,\text{ref}}|}{\sum_j |u_{j,ref}|} \qquad \text{for} \quad j = \{\dots_{1,F_1}, \dots_{2,F_1}, \dots_{1,F_2}, \dots_{2,F_2}\}. \tag{52}$$

Therefore, the completed displacement measure is calculated as

$$u_\text{comp} := \sum_i \frac{|u_i|}{|u_{i,\text{ref}}|} \cdot \frac{|u_{i,\text{ref}}|}{\sum_j |u_i|} = \frac{\sum_i |u_i|}{\sum_j |u_{i,\text{ref}}|} \qquad \text{for} \quad i,j = \{\dots_{1,F_1}, \dots_{2,F_1}, \dots_{1,F_2}, \dots_{2,F_2}\}. \tag{53}$$

Relative time-adjusted nodal displacement error For this measure the nodal displacements of the reference solution are not evaluated at the end time of the analysis. They are instead evaluated at the last converged time points t_last for each solid-void analysis. For this purpose, the reference solution results are interpolated linearly over time to be evaluated exactly at t_last. The interpolated nodal displacements are referred to as $u_{i,\text{ref}}(t_\text{last})$ in the following. This procedure eliminates the influence of not completing the analysis in this error measure, leaving only the error due to a different system behavior at t_{last}. The relative time-adjusted nodal displacement error measure is calculated as

$$u_{\text{error}} := \frac{\sum_i |u_i - u_{i,\text{ref}}(t_{\text{last}})|}{\sum_j |u_{j,ref}(t_{\text{last}})|} \qquad \text{for} \quad i,j = \{\, \dots_{1,F_1}, \, \dots_{2,F_1}, \, \dots_{1,F_2}, \, \dots_{2,F_2} \,\}. \tag{54}$$

3.1.3 | Parametric study results

The results for each of these measures is visualized as a heat map plot over the hyperelastic stabilization parameters C_κ and $\frac{1}{D_2}$ over the range of $10^{-13} \cdots 10^0$ in Table 3 for the 2D model and in Table 4 for the 3D model. The desirable values are

TABLE 3 Parametric study for stabilization parameters calibration using the 2D element types shown in Table 2 for the solid-void structure.

	t_{comp}	u_{comp}	u_{error}
CPS3	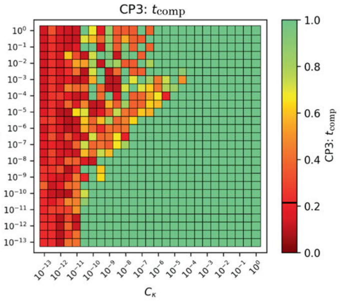	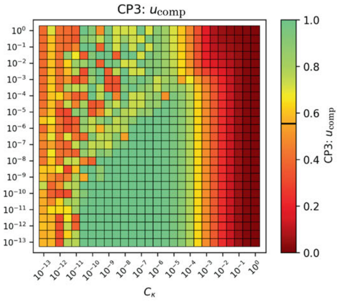	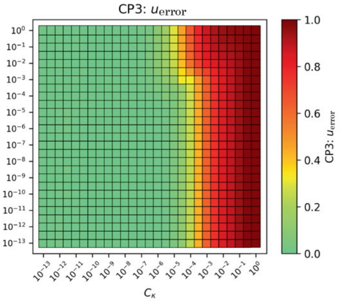
CPS6	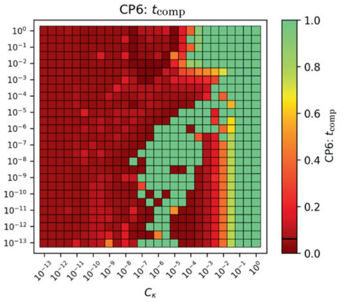	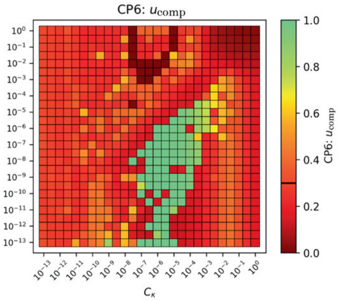	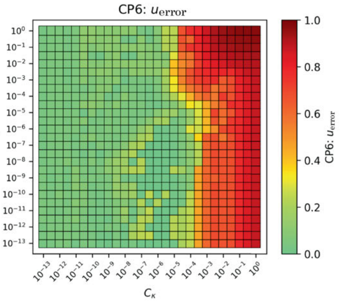
CPS4	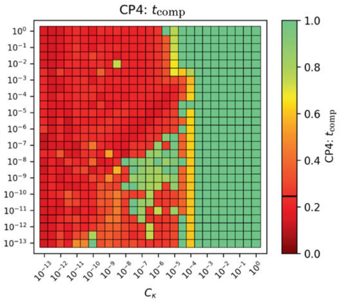	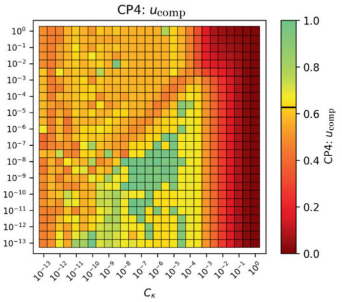	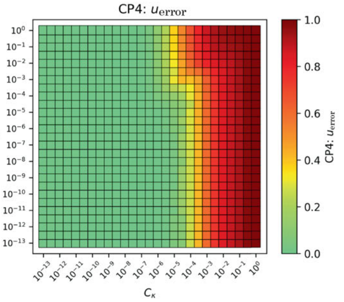
CP4SR	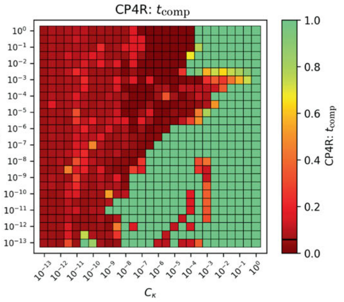	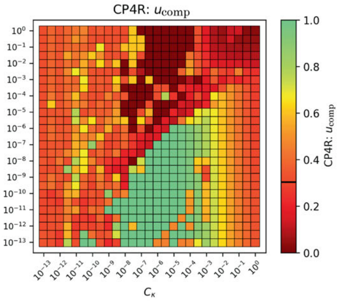	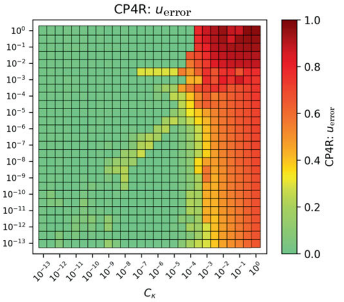

Note: The evaluation measures t_{comp}, u_{comp} and u_{error} are defined in Section 3.1.2.

TABLE 4 Parametric study for stabilization parameters calibration using the 3D element types shown in Table 2 for the solid-void structure.

	t_{comp}	u_{comp}	u_{error}
C3D4	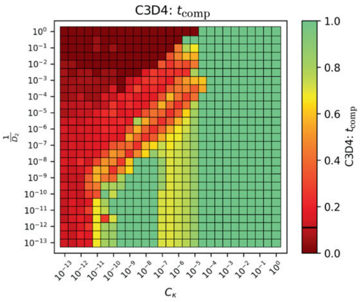	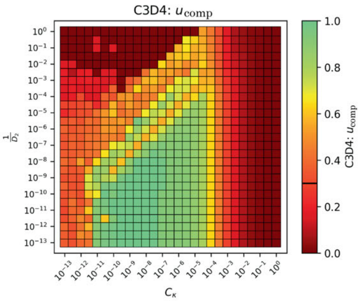	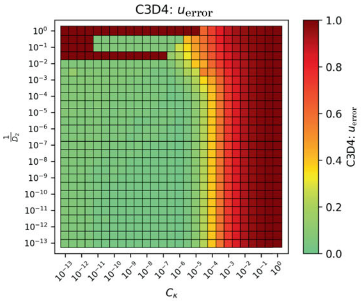
C3D10	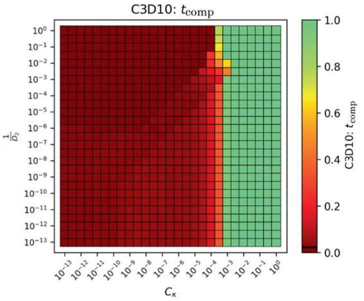	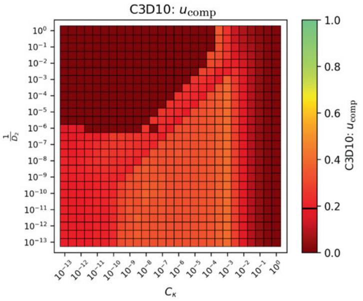	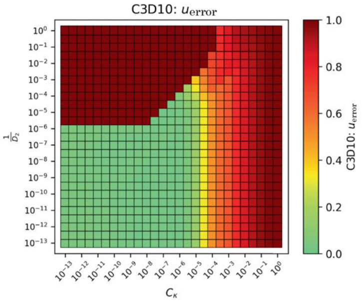
C3D8	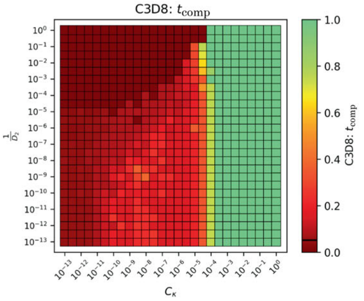	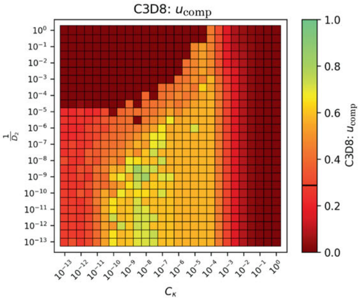	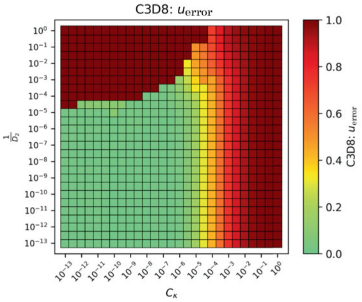
C3D8R	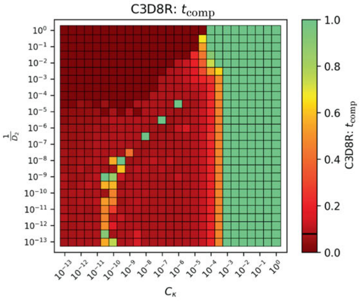	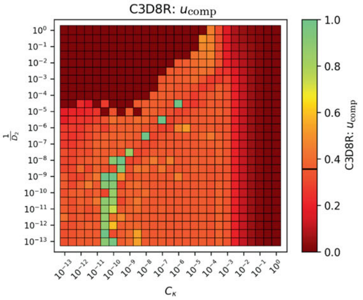	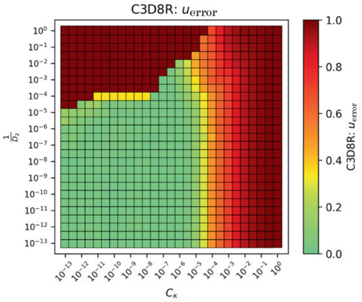

Note: The evaluation measures t_{comp}, u_{comp} and u_{error} are defined in Section 3.1.2.

color-coded green and undesirable values red. In addition, the values of the measures for the non-stabilized solid-void models are shown as black lines in the color bar of the heat map plots. Therefore, values better than these lines represent the improvement achieved by the stabilization scheme. Additionally, the deformed meshes of the solid-only, non-stabilized solid-void and stabilized solid-void analyses are shown in Table 5 for the 2D model and in Table 6 for the 3D model. For these, one of the parameter combinations achieving the best evaluation measures for a given element type is chosen.

A parameter region that improves all three measures to the best possible value for the chosen setup is observed for all 2D element types. This region is especially large for trilateral CP3 elements. The measures are also improved for all tested 3D elements, although the best possible measure is only achieved by C3D4 and C3D8R elements. Especially

TABLE 5 Deformed configurations of the 2D C-shaped structure as solid-only, non-stabilized and stabilized solid-void structure for the 2D element types shown in Table 2.

<table>
<tr><th></th><th>Solid-only-structure
(reference)</th><th>Solid-void-structure
(non-stabilized)</th><th colspan="2">Solid-void-structure
(non-stabilized)</th></tr>
<tr><td rowspan="3">CPS3</td><td rowspan="2">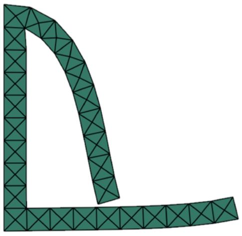</td><td rowspan="2">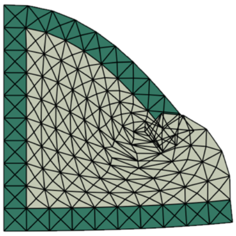</td><td colspan="2">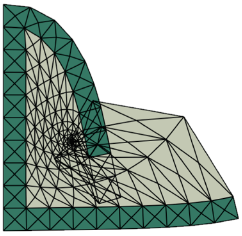</td></tr>
<tr><td>$C_\kappa = 10^{-6}$</td><td>$D_2 = 10^8$</td></tr>
<tr><td>$t_{\text{comp}} = 100.00\%$</td><td>$t_{\text{comp}} = 21.42\%$</td><td colspan="2">$t_{\text{comp}} = 100.00\%$</td></tr>
<tr><td rowspan="3">CPS6</td><td rowspan="2">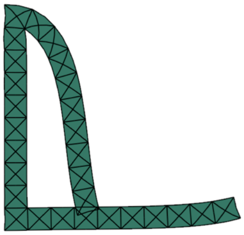</td><td rowspan="2">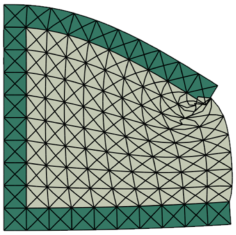</td><td colspan="2">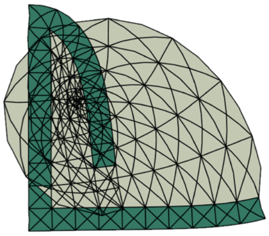</td></tr>
<tr><td>$C_\kappa = 10^{-6}$</td><td>$D_2 = 10^8$</td></tr>
<tr><td>$t_{\text{comp}} = 100.00\%$</td><td>$t_{\text{comp}} = 6.15\%$</td><td colspan="2">$t_{\text{comp}} = 100.00\%$</td></tr>
<tr><td rowspan="3">CPS4</td><td rowspan="2">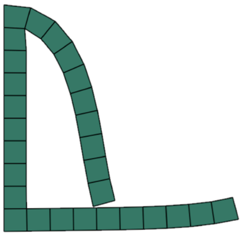</td><td rowspan="2">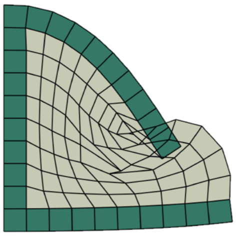</td><td colspan="2">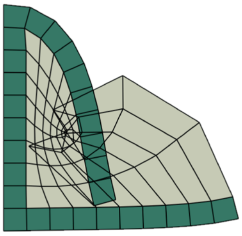</td></tr>
<tr><td>$C_\kappa = 10^{-6}$</td><td>$D_2 = 10^8$</td></tr>
<tr><td>$t_{\text{comp}} = 100.00\%$</td><td>$t_{\text{comp}} = 24.53\%$</td><td colspan="2">$t_{\text{comp}} = 100.00\%$</td></tr>
<tr><td rowspan="3">CPS4R</td><td rowspan="2">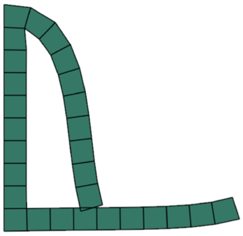</td><td rowspan="2">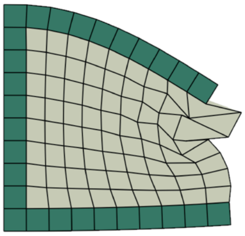</td><td colspan="2">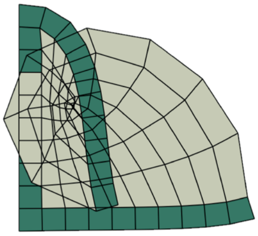</td></tr>
<tr><td>$C_\kappa = 10^{-6}$</td><td>$D_2 = 10^8$</td></tr>
<tr><td>$t_{\text{comp}} = 100.00\%$</td><td>$t_{\text{comp}} = 5.87\%$</td><td colspan="2">$t_{\text{comp}} = 100.00\%$</td></tr>
</table>

Note: Each mesh represents the last converged state of the analysis, which is not necessarily the full loading.

TABLE 6 Deformed configurations of the 3D C-shaped structure as solid-only, non-stabilized and stabilized solid-void structure for the 3D element types shown in Table 2.

	Solid-only-structure (reference)	Solid-void-structure (non-stabilized)	Solid-void-structure (non-stabilized)
C3D4	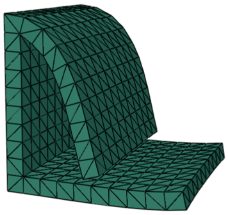	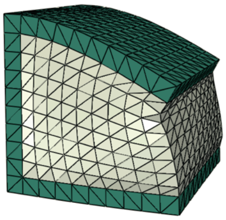	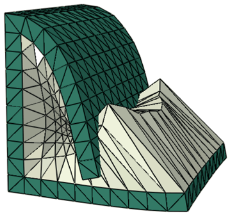 $C_\kappa = 10^{-8.5}$ $D_2 = 10^{11}$
	$t_{\text{comp}} = 100.00\%$	$t_{\text{comp}} = 10.90\%$	$t_{\text{comp}} = 100.00\%$
C3D10	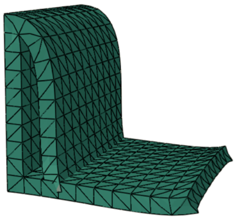	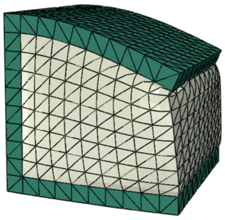	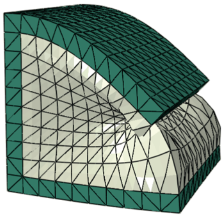 $C_\kappa = 10^{-8}$ $D_2 = 10^{10}$
	$t_{\text{comp}} = 100.00\%$	$t_{\text{comp}} = 2.23\%$	$t_{\text{comp}} = 4.97\%$
C3D8	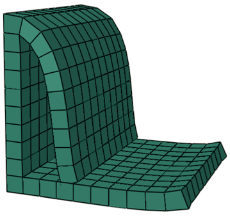	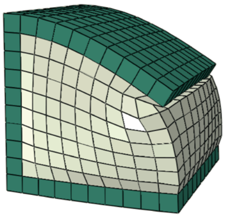	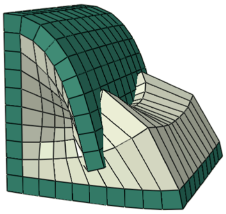 $C_\kappa = 10^{-8}$ $D_2 = 10^{9.5}$
	$t_{\text{comp}} = 100.00\%$	$t_{\text{comp}} = 5.19\%$	$t_{\text{comp}} = 38.27\%$
C3D8R	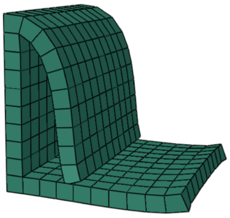	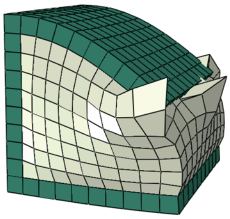	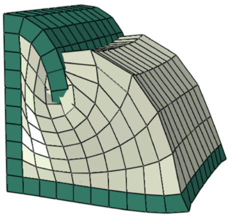 $C_\kappa = 10^{-10.5}$ $D_2 = 10^{9.5}$
	$t_{\text{comp}} = 100.00\%$	$t_{\text{comp}} = 7.79\%$	$t_{\text{comp}} = 100.00\%$

Note: Each mesh represents the last converged state of the analysis, which is not necessarily the full loading.

the tetrahedral C3D4 elements have a significantly improved numerical stability ($\Delta u_{\text{comp}} = 67\%$) and a large parameter region, in which the improvement is achieved.

The u_{error} plots show that values for $C_\kappa \geq 10^{-4}$ start to significantly affect the system behavior. This is similar to the findings of an upper bound on the void stiffness recommended in References 30 and 11.

Some non-feasible parameter combinations were observed in the upper left corner. These parameter combinations yield a close to incompressible constitutive law and would require a hybrid element formulation. These were not further investigated, since their neighboring parameter combinations did not indicate a parameter region that would improve the numerical stability.

3.2 | Geometrically nonlinear topology optimization results

This section addresses the calibration and verification of the stabilization material model for topology optimization considering large deformations using both academic models[7,11] as well as industrial application models. All optimizations are conducted without any continuation scheme or incremental projection scheme for the filtering or material interpolation.

3.2.1 | Cantilever beam

The cantilever beam has the dimensions 1 [m] × 0.25 [m] × 0.1 [m] and is fully constrained on the left side. The load P is applied at the reference point (RP) as shown in Figure 6. The cantilever beam is discretized using 120 × 30 CPE4 plane strain elements.[28] The material of the cantilever beam is modeled once as linear elastic model having a Young's modulus of $E = 3$ [GPa] and a Poisson's ration of $\nu = 0.4$ and once as elastoplastic model having the same elastic properties as well as a yield stress of $Y = 9$ [MPa] and a yield hardening of $H = 0.02 \cdot E = 60$ [MPa] (2% of the initial Young's modulus). The optimization setup is defined as

$$\min_{\rho \in \varrho} \quad y_{\text{RP}}, \tag{55}$$

$$s.t. \quad V \leq 0.5 \cdot V_0, \tag{56}$$

where y_{RP} is the vertical displacement of the reference point (RP), V the current volume and V_0 the reference volume. The model is stabilized by applying the strain energy density function

$$U = S \cdot E \cdot \left(\left(\bar{I}_1 \bar{I}_2 - 9 \right) + \frac{1}{100} \cdot \left(J^{\text{el}} - 1 \right)^4 \right) \tag{57}$$

for the elastic cantilever beam model and

$$U = S \cdot H \cdot \left(\left(\bar{I}_1 \bar{I}_2 - 9 \right) + \frac{1}{100} \cdot \left(J^{\text{el}} - 1 \right)^4 \right), \tag{58}$$

for the elastoplastic cantilever beam model, where E and H are the physical stiffness properties and S is a scaling factor that is varied in the following numerical experiments. This definition is equivalent to a line search through the stabilization parameter space shown in the previous section. The relative factor 1/100 between C_κ and D_2 is chosen based on the results

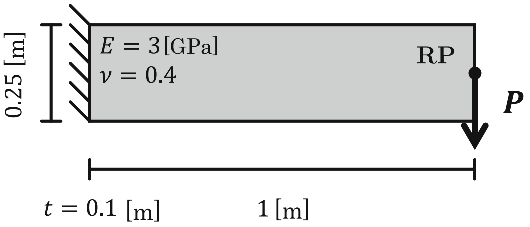

FIGURE 6 Cantilever beam model.

from the previous section to conduct the line search through the most promising region of the parameter space. When expressed in the form of (47), the effective stabilization parameters are

$$C_\kappa = S \cdot E, \tag{59}$$

$$D_2 = \frac{100}{S \cdot E}, \tag{60}$$

for the elastic cantilever beam model and

$$C_\kappa = S \cdot H, \tag{61}$$

$$D_2 = \frac{100}{S \cdot H}, \tag{62}$$

for the elastoplastic cantilever beam model. In the following, the load factor P as well as the stabilization factor S are varied and the optimizations are compared in terms of divergence of the primal solution. Afterwards, a selection of representative optimized models is compared to their corresponding validation model, for which the stabilization elements as well as void elements below $\rho < 0.05$ are removed from the analysis. Removal of the void elements is necessary, since numerical instabilities in void element regions is still present, even in the optimized designs.

Elastic cantilever beam results

The optimized design layouts for the elastic cantilever beam are shown in Table 7. The non-stabilized elastic cantilever beam model exhibits numerical instabilities for loads $P \geq 125$ [kN] causing the optimization to fail after a few optimization iterations. Converges of the primal solution for higher load factors throughout the entire optimization is achieved by increasing the stabilization factor S. A clear correlation between increased stabilization factor and loads for which the optimization converged is observed. Note, that this observation does not take into account the physical accuracy of the model. For example, the highest stabilization factor of $S = 10^{-3} \cdot E$ clearly shows non-physical designs, indicating that the stabilization elements contribute significantly to the total system behavior. Therefore, the converged optimizations applying the highest load factor for each stabilization factor are investigated further in terms of physical accuracy. The comparison between the stabilized model and the respective validation model is shown in Table 8. For stabilization factors up to $S = 10^{-5} \cdot E$ no significant difference between the stabilized model and the validation model is observed. In contrast, the comparison for higher stabilization factors shows a significant difference between the two models, although the qualitative system behavior is unchanged. Therefore, the stabilization factor should not exceed $S = 10^{-5} \cdot E$ if physical accuracy is required. If higher stabilization factors are chosen, we advise a validation of the optimized design to ensure that the qualitative system response was not significantly affected by the stabilization elements.

TABLE 7 Optimized design layouts for the elastic cantilever beam applying different loads P [kN] and stabilization factors S for (57) being expressed in terms of the material's elastic Young's modulus E.

P [kN]	$S = 0$	$S = 10^{-7} \cdot E$	$S = 10^{-6} \cdot E$	$S = 10^{-5} \cdot E$	$S = 10^{-4} \cdot E$	$S = 10^{-3} \cdot E$
0.001						
100						
125						
150						
200						
300						
500						

TABLE 8 Elastic cantilever beam validation results for different stabilization factors S and loads P comparing the stabilized models of optimized designs with their respective validation models, in which the stabilization elements as well as void element below $\rho \leq 0.05$ are removed from the analysis.

		Stabilized model			Validation model			Comparison			
P [kN]	S [e]	x_{RP} [mm]	y_{RP} [mm]	c $\left[\frac{\text{mm}}{\text{kN}}\right]$	x_{RP} [mm]	y_{RP} [mm]	c_V $\left[\frac{\text{mm}}{\text{kN}}\right]$	$\frac{\Delta x_{\text{RP}}}{x_{\text{RP}}}$ [%]	$\frac{\Delta y_{\text{RP}}}{y_{\text{RP}}}$ [%]	$\frac{\Delta c}{c}$ [%]	$\frac{U_{\text{Stab}}}{U_{\text{Tot}}}$ [%]
125	10^{-7}	−16.804	−140.027	1.120216	−16.805	−140.029	1.120232	< 0.1%	< 0.1%	< 0.1%	< 0.1%
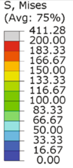		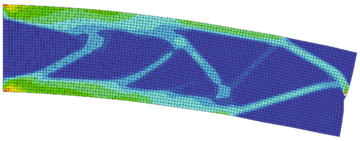			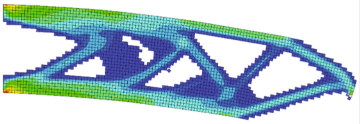			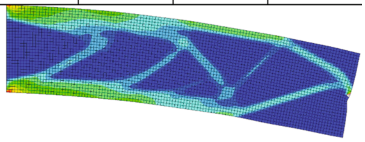			
150	10^{-6}	−45.335	−161.716	1.078106	−45.449	−161.709	1.07806	0.2%	< 0.1%	< 0.1%	< 0.1%
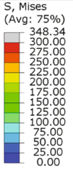		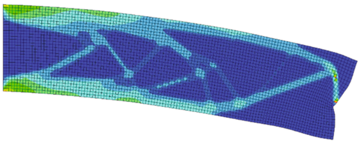			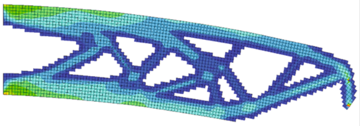			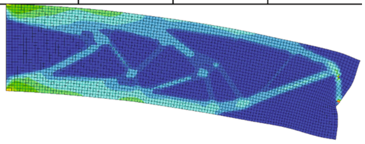			
200	10^{-5}	−92.078	−212.541	1.062705	−94.375	−212.156	1.06078	−2.4%	0.18%	0.18%	< 0.1%
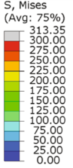		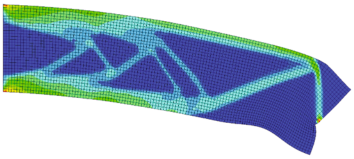			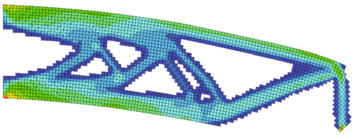			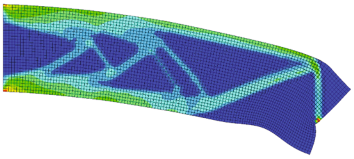			
300	10^{-4}	−179.942	−316.231	1.054103	−203.78	−311.87	1.039566	−11.7%	1.40%	1.40%	6.29%
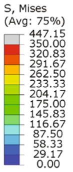		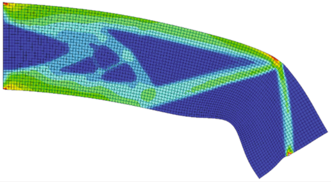			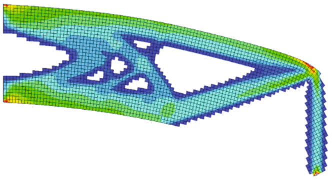			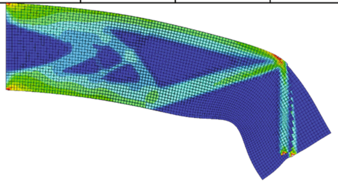			
500	10^{-4}	−335.629	−453.453	0.906906	−360.058	−448.366	0.896732	−6.78%	1.13%	1.13%	7.33%
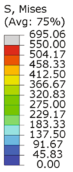		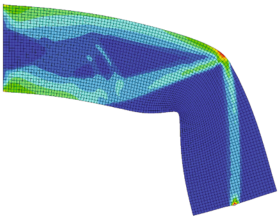			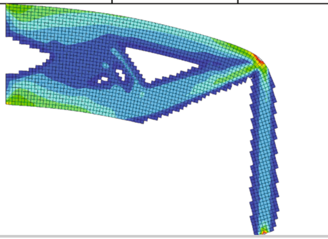			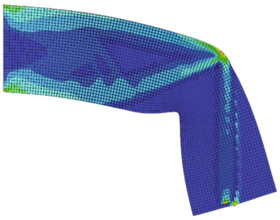			

Note: The deformed meshes and von Mises stresses are shown for the stabilized model, the validation model and as overlay of the two. The stresses for each row are scaled to the same color scale. The numerical values for the reference point displacements x_{RP} and y_{RP} as well as the compliance c are given. Furthermore, the relative difference $\frac{\Delta x_{\text{RP}}}{x_{\text{RP}}}$, $\frac{\Delta y_{\text{RP}}}{y_{\text{RP}}}$ and $\frac{\Delta c_{\text{RP}}}{c}$ normalized with respect to the corresponding validation model value are calculated. Lastly, $\frac{U_{\text{stab}}}{U_{\text{Tot}}}$ as the relative strain energy in the stabilization elements with respect to the total elastic strain energy in the model is calculated for the stabilized model.

Elastoplastic cantilever beam results

The optimized design layouts for the elastoplastic cantilever beam are shown in Table 9. The non-stabilized elastic cantilever beam model exhibits numerical instabilities for loads $P \geq 10$ [kN]. As for the elastic model, including stabilization ensures the convergence of the optimizations for higher load amplitudes. An increased stabilization factor again correlates to an increase of the highest load factor for which the optimization converged. Even including a very small stabilization factor $S = 10^{-9} \cdot H$ in the model ensures the convergence of the optimization for a higher load amplitude than for the non-stabilized model. Representative optimized designs are further investigated in terms of numerical accuracy as shown in Table 10. The comparison between the stabilized models and the respective validation models is shown in Table 10. All tested optimized designs except the one applying the highest stabilization factor show no significant difference between

TABLE 9 Optimized design layouts for the elastoplastic cantilever beam applying different loads P [kN] and stabilization factors S for (58) being expressed in terms of the hardening stiffness $H = 0.02 \cdot E$, where E is the elastic Young's modulus.

P [kN]	$S = 0$	$S = 10^{-9} \cdot H$	$S = 10^{-6} \cdot H$	$S = 10^{-5} \cdot H$	$S = 10^{-4} \cdot H$	$S = 10^{-3} \cdot H$
0.001						
4						
9						
10						
12						
15						
25						

the stabilized models and the validation models. Hence, the stabilization scheme stabilizes the optimization for significantly higher load amplitudes without significantly affecting the system behavior. The significant design difference for the model applying $P = 25$ [kN] and $S = 10^{-3} \cdot H$ shows the issue arising, if the stabilization factor is chosen too high. A beam member in the design did not exhibit buckling in the optimized stabilized model, but did exhibit buckling in the corresponding validation model. Therefore, a too high stabilization can prevent buckling, while a sufficiently low scaled stabilization factor does not. The buckling of this beam member also explains the qualitative difference in the optimized designs for high load amplitudes when compared to the optimized designs of the elastic cantilever beam model. The elastic cantilever beam models include a hinge mechanism that is located at the top of the design domain, while the elastoplastic cantilever beam models have a similar hinge mechanism at the bottom of the design space. This is due to the beam that is located underneath the hinge in the elastic design exceeding its buckling load for the elastoplastic cantilever beam model. Hence, the designs of the elastoplastic cantilever beam model include a thicker and shorter beam in the horizontal orientation and a diagonal beam above, which is loaded in tension and can therefore, not buckle.

The stabilization factor is scaled with respect to H instead of E for two reasons. First, the elements exhibiting numerical instabilities will undergo large strains often far beyond the yield strain of most physical materials that can be described by elastoplastic constitutive theory. Therefore, the tangent stiffness of numerically unstable elements is equivalent to the terminal yielding stiffness. Second, physical elements having an intermediate density and experiencing yielding decrease their tangent stiffness by at least one order of magnitude, while still having a significant effect on the physical system behavior. Therefore, stabilization stresses being scaled to the initial tangent stiffness E instead of H would dominate stresses in the yielding of the intermediate density elements. This can lead to the suppression of buckling modes for thin members of the optimized design as observed for the optimization applying the highest stabilization factor and load factor. The recommended scaling parameter $S = 10^{-5} \cdot E$ for the elastic constitutive material modeling would be equivalent to the scaling factor $S = 5 \times 10^{-4} \cdot H$ for the elastoplastic constitutive material modeling, which is in the range for which a significant effect of the stabilization on the physical system response was observed for the elastoplastic cantilever beam model. Therefore, we recommend the stabilization factor $S = 10^{-5} \cdot H$ for elastoplastic constitutive material model.

3.2.2 | Double clamped beam

The system shown in Figure 7 is another benchmark example from the Reference 7 showing a snap-through behavior of the optimized design for higher loads when considering geometrically nonlinear modeling. The beam has the dimensions 3 [m] × 1 [m] × 0.1 [m] and is discretized using 120 × 40 CPE4 plane strain elements. It is fully constrained on both sides and loaded in the middle with a force $P = 80$ [kN]. The material is modeled as linear elastic having a Young's modulus of

TABLE 10 Elastoplastic cantilever beam validation results for different stabilization factors S and loads P comparing the stabilized models of optimized designs with their respective validation models, in which the stabilization elements as well as void elements below $\rho \leq 0.05$ are removed from the analysis.

		Stabilized model			Validation model			Comparison			
P [kN]	S [H]	x_{RP} [mm]	y_{RP} [mm]	c $\left[\frac{\mathrm{mm}}{\mathrm{kN}}\right]$	x_{RP} [mm]	y_{RP} [mm]	c_V $\left[\frac{\mathrm{mm}}{\mathrm{kN}}\right]$	$\frac{\Delta x_{\mathrm{RP}}}{x_{\mathrm{RP}}}$ [%]	$\frac{\Delta y_{\mathrm{RP}}}{y_{\mathrm{RP}}}$ [%]	$\frac{\Delta c}{c}$ [%]	$\frac{U_{\mathrm{Stab}}}{U_{\mathrm{Tot}}}$ [%]
10	10^{-9}	-0.0707	-11.098	1.10979	-0.0707	-11.098	1.10979	< 0.1	< 0.1	< 0.1	< 0.1
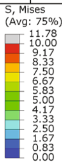		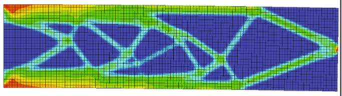			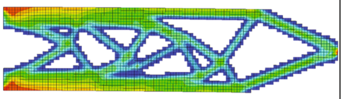			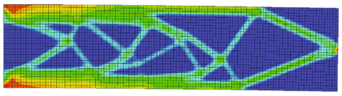			
12	10^{-6}	-0.285	-14.032	1.169333	-0.283	-14.033	1.1694	0.73	< 0.1	< 0.1	< 0.1
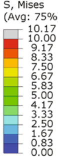		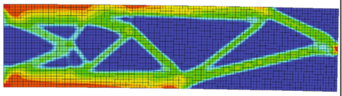			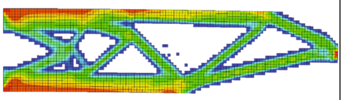			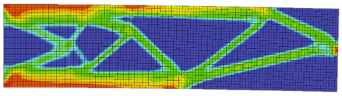			
15	10^{-6}	-104.631	-170.976	11.398	-104.89	-171.03	11.402	-0.24	< 0.1	< 0.1	< 0.1
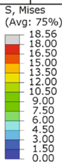		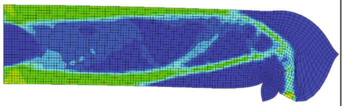			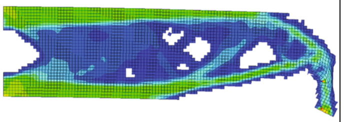			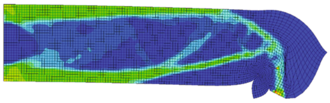			
15	10^{-5}	-80.112	-143.229	9.5486	-81.097	-142.933	9.528	-1.21	0.207	0.207	< 0.1
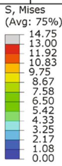		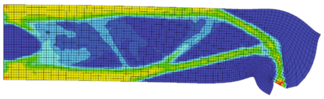			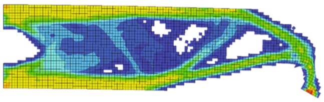			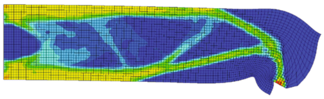			
15	10^{-4}	-0.702	-22.017	1.467826	-0.699	-22.031	1.4687	0.38	< 0.1	< 0.1	< 0.1
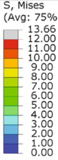		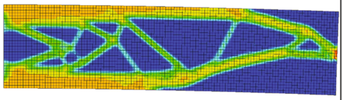			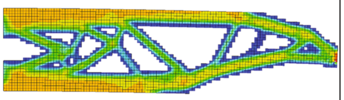			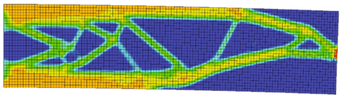			
25	10^{-5}	-308.288	-470.798	18.83192	-309.112	-470.484	18.81936	-0.2	< 0.1	< 0.1	0.116
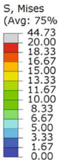		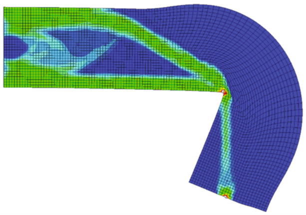			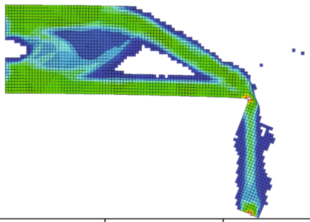			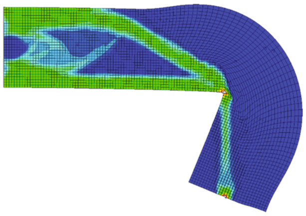			
25	10^{-3}	-220.41	-337.079	13.483	-267.458	-358.252	14.330	-17.59	-5.91	-5.91	0.761
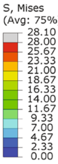		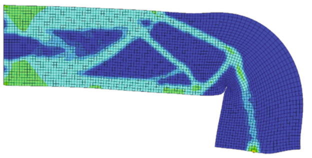			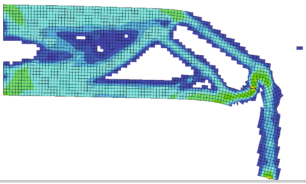			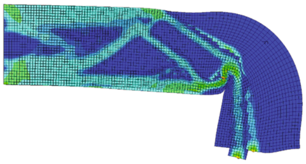			

Note: The deformed meshes and von Mises stresses are shown for the stabilized model, the validation model and as overlay of the two. The numerical values for the reference point displacements x_{RP} and y_{RP} as well as the compliance c are given. Furthermore, the relative difference $\frac{\Delta x_{\mathrm{RP}}}{x_{\mathrm{RP}}}$, $\frac{\Delta y_{\mathrm{RP}}}{y_{\mathrm{RP}}}$ and $\frac{\Delta c_{\mathrm{RP}}}{c}$ normalized with respect to the corresponding validation model value are calculated. Lastly, $\frac{U_{\mathrm{stab}}}{U_{\mathrm{Tot}}}$ as the relative strain energy in the stabilization elements with respect to the total elastic strain energy in the model is calculated for the stabilized model.

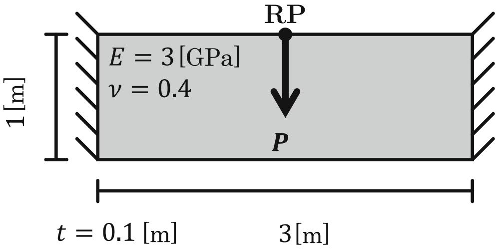

FIGURE 7 Double clamped beam model.

$E = 3$ [GPa] and a Poisson ratio of $\nu = 0.4$. The optimization defined as

$$\min_{\rho \in \varrho} \quad y_{\mathrm{RP}}, \tag{63}$$

$$s.t. \quad V \leq 0.1 \cdot V_0, \tag{64}$$

minimizing the vertical displacement y_{RP} of the loading point subject to a volume constraint of 10%. Such a low volume fraction causes a problem for the optimization. The homogeneous initial design consisting of a 10% uniform material distribution and the following first optimization iterations all exhibit large deformations for very few elements around the loading point causing the finite element analysis to diverge. Until now this problem was solved in literature by applying a continuation scheme, where the material penalization factor p was slowly increased from 1 to 3. This requires many optimization iterations and is based on a heuristic updating scheme. We instead apply the stabilization scheme in this article to stabilize this optimization. The challenge here is to stabilize the first few iterations without affecting the physical system behavior significantly. We apply the stabilization strain energy potential defined in (57) using $S = 10^{-5} \cdot E$. The optimization converged smoothly in only 45 optimization iterations as shown in Figure 8B. References 7 and 11 applied a continuation scheme to optimize this model and reported 125 and 600 optimization iterations, respectively. The optimized design is shown in Figure 8A. Figure 8C shows the relative strain energy of the stabilization elements with respect to the total strain energy of the system. During the first few optimization iterations this ratio is very high, since the stabilization is required to stabilize the model during the first few optimization iterations. During the optimization iterations this value decreases smoothly until its relative value is below 1%. Note, that this decrease is not related to the decrease in compliance of the overall model, since it is a relative measure taking into account the overall compliance. A validation run of the optimized model for which the stabilization elements as well as low-density elements below $\rho = 0.05$ are removed from the analysis shows no difference in system behavior. Therefore, the stabilization did not change or stabilize the physical buckling behavior. The deformed meshes and stressed for the initial and optimized design as well as the validation model are shown in Figure 9. Optimizations applying higher loads P and the same stabilization factor S exhibited a global buckling during the optimization process causing the optimization to fail. Therefore, the applied stabilization factor does not suppress global buckling modes if they are present.

3.2.3 | Three-point bending beam

This model shown in Figure 10 is a dynamic impact analysis of a rigid punch which hits an elastoplastic beam in a three-point bending beam setup including all three types of non-linearities: geometrical, material and contact.

The beam is placed on two supports and impacted by a punch in the middle. The supports are fully constrained, while the punch can move freely in the vertical direction. The contact between the parts is modeled using finite sliding as well as friction having a friction coefficient of $\mu = 0.1$ in all contact interfaces. Both the supports as well as the punch are modeled as rigid. In addition, the punch is assigned a mass of $m = 200$ [kg] and an initial velocity $v_0 = 10$ [m/s]. The beam is modeled as elastoplastic using a Young's modulus of $E = 70$ [GPa] and a Poisson's ratio of $\nu = 0.33$ as well as a yield stress of $Y = 311$ [MPa] having an isotropic hardening of $H = 0.02 \cdot E$. The model is reduced to a quarter model by applying symmetry. The quarter beam is discretized using 13,482 linear brick elements (C3D8). The model is stabilized by applying the hyperelastic strain energy potential from (58) using $S = 10^{-5} \cdot H$. The optimization minimizes the maximal

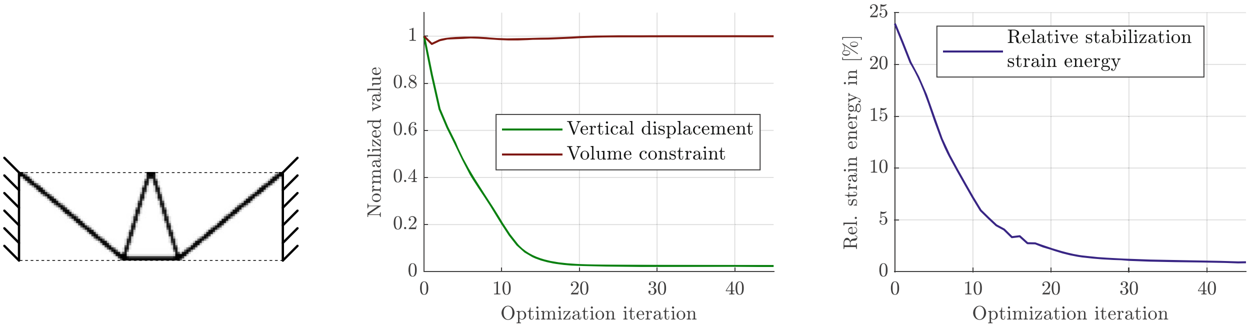

(a) **(b)** **(c)**

FIGURE 8 Double clamped beam (A) optimized design layout applying a load of $P = 80$ [kN], (B) optimization iteration history and (C) relative strain energy of the stabilization elements with respect to the total systems strain energy for each optimization iteration.

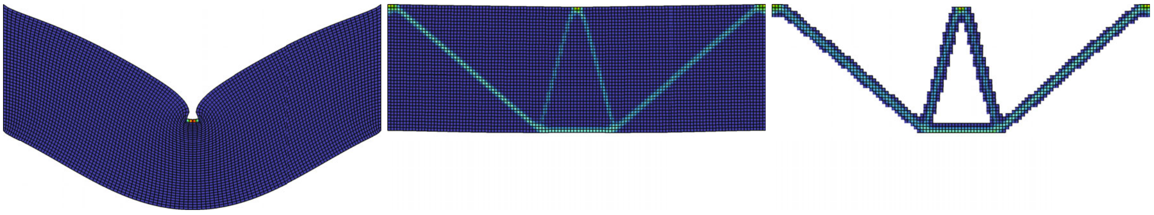

(a) **(b)** **(c)**

FIGURE 9 Deformed meshes and von Mises stresses of the double clamped beam model for (A) the initial design and (B) the optimized design, both applying the stabilization parameters $C_\kappa = 10^{-5} \cdot E$ and $D_2 = 10^7 \cdot 1/E$ as well as (C) the validation model of the optimized design, for which the stabilization elements as well as void elements below $\rho \leq 0.05$ are removed from the analysis.

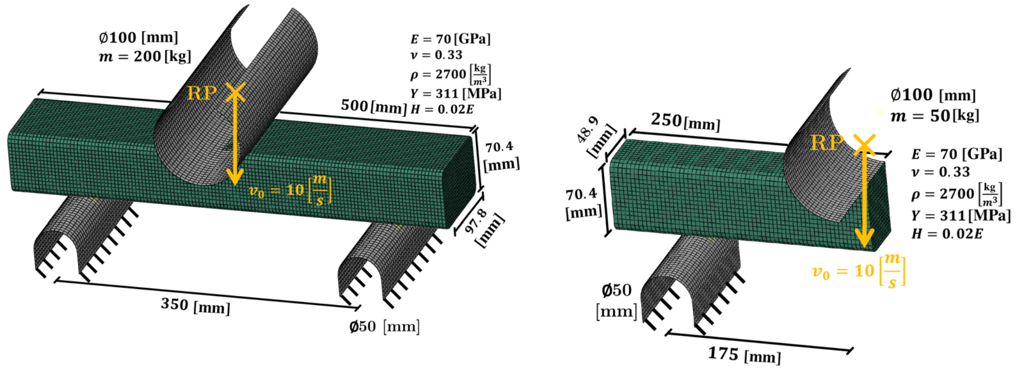

(a) **(b)**

FIGURE 10 Three-point bending beam (A) model and (B) a quarter model reduced using symmetry.

vertical displacement of the punch over the analysis time subject to a volume constraint of 30% as follows

$$\min_{\rho \in \varrho} \quad \max(u_{\mathrm{RP}}(t_i)), \tag{65}$$

$$s.t. \quad V \leq 0.3 \cdot V_0, \tag{66}$$

$$t_i \in \{0.001, 0.002, \ldots, 0.025\} \text{ [s]}. \tag{67}$$

The optimization converged in 73 iterations as shown in Figure 11A. The vertical displacement of the punch's reference point is decreased by 88.3% while satisfying the volume constraint of 30%. The optimized design layout is shown in

Figure 11B as well as a corresponding isosurface enforcing the volume fraction of 30%. The extent of the large deformation and sliding in the interfaces in this model is evident when comparing the deformed meshes of the initial and optimized designs in Figure 12A,B. The initial design does not stop the punch at all and the beam is pushed completely through the two supports, while the optimized design catches the punch. Therefore, this optimization requires large deformation modeling to capture the correct physics. A validation model is derived from the optimized design for which the stabilization elements as well as elements having a density of $\rho \leq 0.05$ are removed from the model. The displacement of the reference point for the optimized stabilized model and the validation model are then compared and shown in Figure 13B. No significant difference between the two models is observed. Furthermore, the relative strain energy of the stabilization elements with respect to the total strain energy is below 1% for the optimized design (see Figure 13A), having a value of 0.98% in the optimized design. Therefore, it is expected that the physical system behavior is not changed significantly by the stabilization elements. Note, that the relative strain measure for each optimization iteration is evaluated at the time point of maximal vertical displacement of a primal solution. Furthermore, this measure does not consider dissipated plastic energy or kinetic energy. Therefore, it is a very conservative measure for estimating the influence of the stabilization

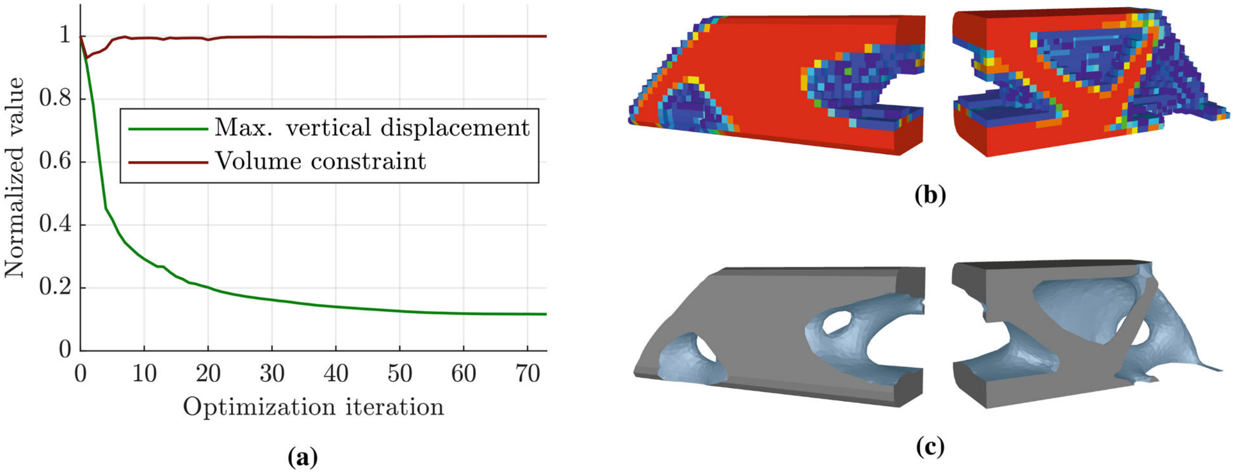

(a)

(b)

(c)

FIGURE 11 Three-point bending beam optimization results showing (A) the optimization iteration history of the normalized maximal vertical displacement of the punch reference point (RP) as well as the normalized volume constraint enforcing a volume fraction of $0.3 \cdot V_0$. (B) The optimized design variable layout from the front (left) and back (right) applying a threshold of $\rho = 0.05$ and (C) the corresponding iso-surfaced generated using the optimized topology and enforcing the volume fraction of $0.3 \cdot V_0$.

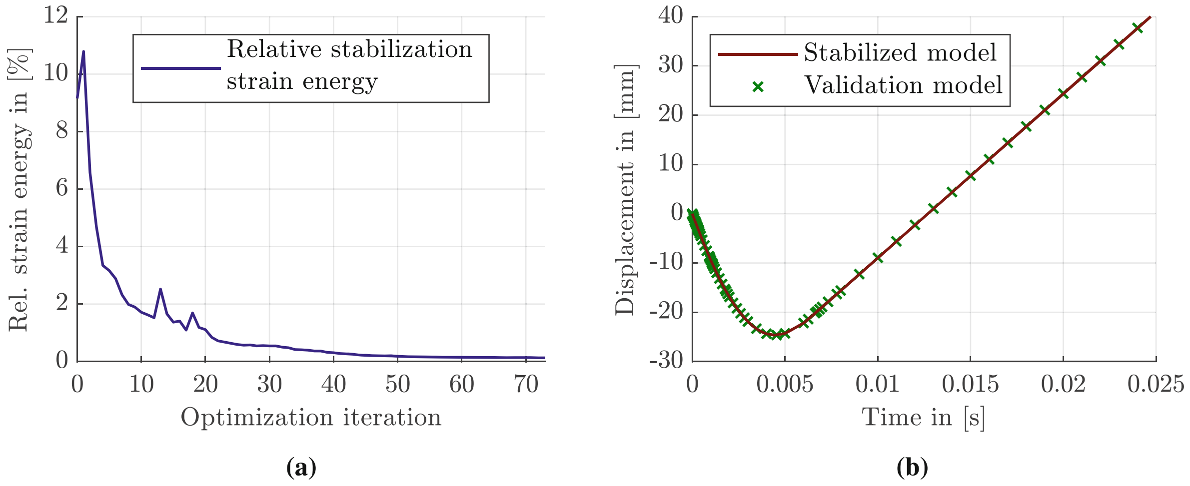

(a)

(b)

FIGURE 12 (A) Relative internal energy of the stabilization elements with respect to the total elastic strain energy in all elements for the stabilized three-point bending beam model shown in Figure 10. (B) Comparison of the reference point (RP) displacement over time t for the optimized stabilized model and the corresponding validation model.

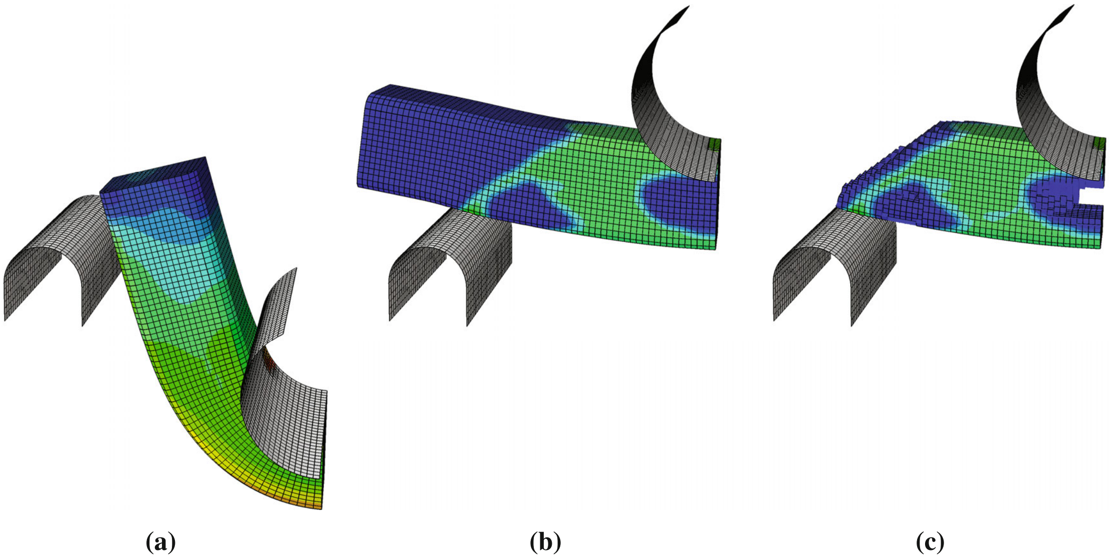
(a) (b) (c)

FIGURE 13 Deformed meshes and von Mises stresses at the time point of maximal displacement for the three-point bending beam model for (A) the initial design, (B) the optimized design and (C) the validation model of the optimized design, for which the stabilization elements as well as void elements below $\rho \leq 0.05$ are removed from the analysis.

elements on the physical system behavior. Optimizations without stabilization were also conducted, but failed in the calculation of the primal solution for optimization iteration 15, thereby, showing the necessity for stabilization of this model to perform the optimization.

3.2.4 | Track rod

A track rod is a part of a car's wheel suspension system. It stabilizes the wheel bearing around the vertical axis during normal driving operations. During an overloading the track rod should absorb and limit the forces that are transmitted to prevent damage to the rest of the wheel suspension system, while retaining a certain structural integrity after a large deformation caused by a misuse. The track rod is discretized as half model by applying symmetry as shown in Figure 14A using 91,653 C3D8R reduced integration linear brick elements. The detailed dimension of the full track rod are given in the appendix Figure B1. The material is assumed to be elastoplastic applying a Young's modulus of $E = 71.5$ [GPa], a Poisson's ratio of 0.33 as well as a yield stress of $Y = 320$ [MPa] having a hardening stiffness of $H = 0.01 \cdot E$. The track rod is analyzed with respect to the two load cases (LC1 and LC2) shown in Figure 14B. The first load case LC1 is a linear analysis, where the structure is loaded with the force $F = 2300$ [N] to evaluate the initial stiffness of the structure. The second load case LC2 is a geometrically nonlinear quasi-static analysis, where the prescribed displacement $x_{\mathrm{RP}}(t) = 20$ [mm/s] $\cdot\, t$ for $t \in [0, 1]$ [s] is applied and the corresponding reaction force response of the structure resulting from the prescribed displacement is evaluated. This load case evaluates the overloading behavior of the structure. The model is stabilized by applying the hyperelastic strain energy potential from (58) using $S = 10^{-5} \cdot H$.

The desired design properties of the track rod are transformed into an initial stiffness constraint as well as an upper and lower reaction force response constraint as shown in Figure 14C. Hence, the optimization incorporates post-buckling properties of the structure. The design space is shown in green in Figure 14A. The optimization minimizes the material volume of the track rod while fulfilling these requirements for LC1 and LC2, yielding

$$\min_{\rho \in \varrho} \quad V, \tag{68}$$

$$s.t. \quad \mathrm{LC1}: x_{\mathrm{RP}} \quad \leq 0.08 \text{ [mm]}, \tag{69}$$

$$s.t. \quad \mathrm{LC2}: \mathrm{RF}(t_i) \quad \leq 50 \text{ [kN]}, \tag{70}$$

$$s.t. \quad \mathrm{LC2}: \mathrm{RF}(1 \text{ [s]}) \quad \geq 15 \text{ [kN]}, \tag{71}$$

$$t_i \in \{0.05, 0.10, \ldots, 1\} \text{ [s]}. \tag{72}$$

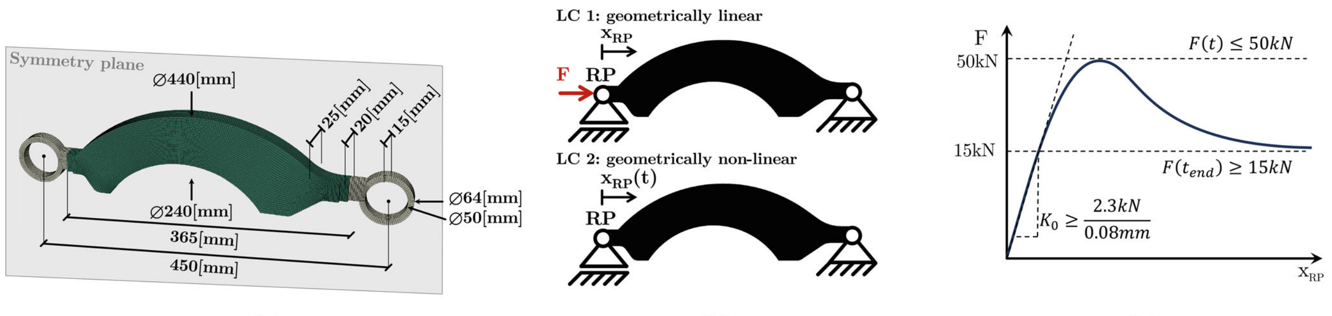

(a) (b) (c)

FIGURE 14 (A) Track rod mesh and dimensions (see Appendix Figure B1 for all dimensions) as well as the design space shown in green. (B) The geometrically linear load case (LC1), where a force F acts at the reference point of the track rod and the geometrically nonlinear load case (LC2, where the reference point of the track rod has a prescribed displacement $X_{\mathrm{RP}}(t)$, which ramps up the displacement linearly to 20 [mm]. (C) The constraints for the force response curve of the track rod imposed by the displacement constraint for the geometrically linear load case and the corresponding reaction force constraints in the geometrically nonlinear load case.

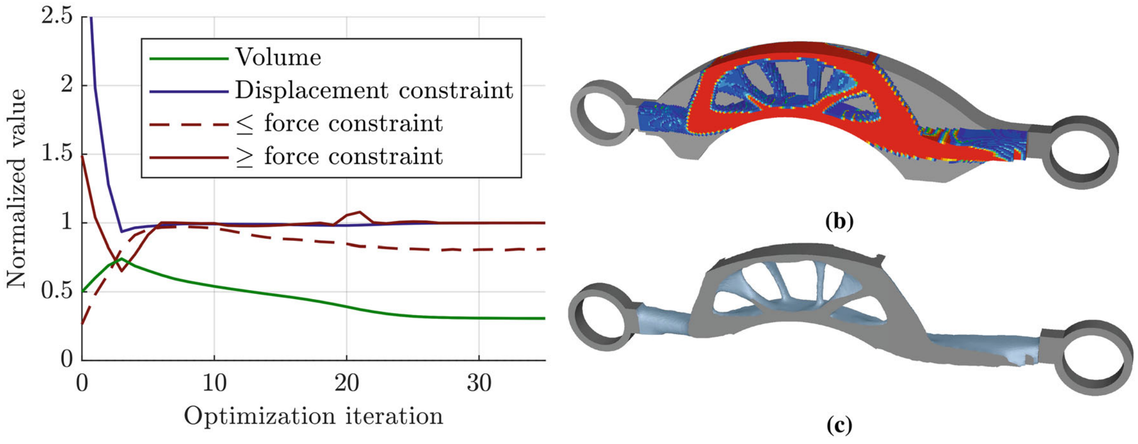

FIGURE 15 (A) Track rod optimization iteration history of the volume objective function, the displacement constraint, as well as the upper and lower reaction force constraints on the reaction force response. (B) Optimized design variable layout of the track rod thresholded at $\rho = 0.05$. (C) Iso-surface generated design by enforcing the volume fraction of the optimized design.

The optimization converged in 35 optimization iterations as shown in Figure 15A, yielding a volume fraction 30.7%, while satisfying all constraints. The initial stiffness constraint as well as the lower force response constraint are active in the optimized design, while the upper force response constraint is not active. The optimized design variable layout is shown in Figure 15B as well as a corresponding isosurface enforcing a volume fraction of 30% shown in Figure 15C. Figure 16A shows that the stabilization elements contribute less than 1% of the total elastic strain energy. Thereby, the stabilization elements prevent divergence of the primal solutions while having an insignificant effect on the physical behavior. A validation model of the optimized design is created, for which the stabilization elements as well as void elements below $\rho = 0.05$ are removed from the analysis. The force response curves of the optimized stabilized model and the validation model are compared in Figure 16B and show no significant difference. The stresses in the deformed configuration are shown for the initial design, the optimized design as well as the validation model in Figure 17. The same optimization was also conducted without applying the stabilization scheme and failed in optimization iteration 24 due to divergence of the primal solution, thereby, proving the need for numerical stabilization in this optimization. The findings from this optimization show that the stabilization scheme can prevent local artificial buckling modes without affecting the physical global buckling modes.

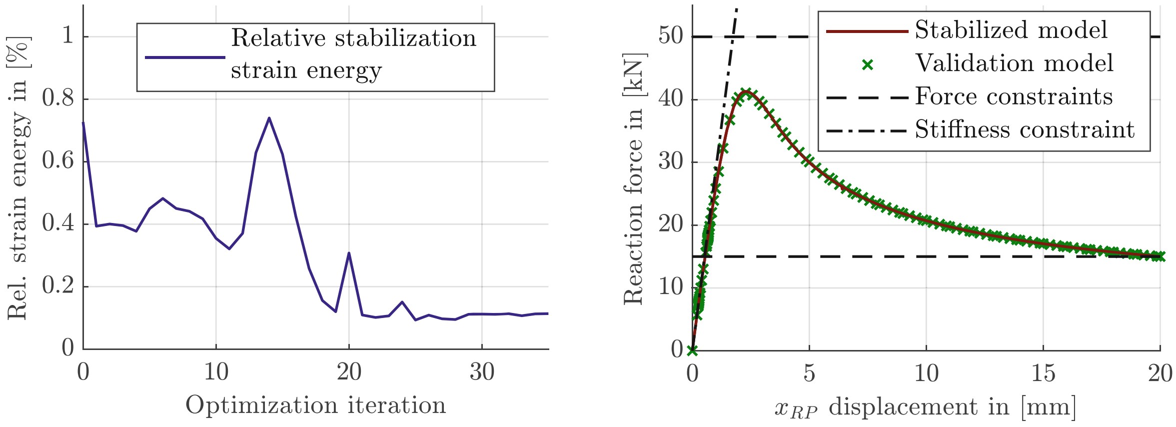

(a) **(b)**

FIGURE 16 (A) Track rod optimization iteration history of the relative stabilization energy with respect to the total elastic strain energy of the system. (B) Comparison of the force-displacement curves of the optimized stabilized model and the corresponding validation model of the track rod, showing no difference between the two models. The validation model is derived by removing the stabilization elements as well as elements below a density of $\rho = 0.05$.

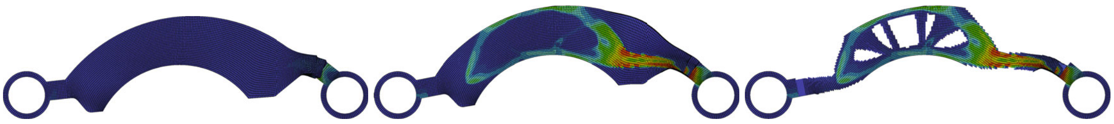

(a) **(b)** **(c)**

FIGURE 17 Deformed meshes and von Mises stresses for the track rod model for (A) the initial design, (B) the optimized design and (C) the validation model of the optimized design, for which the stabilization elements as well as void elements below $\rho \leq 0.05$ are removed from the analysis.

3.2.5 | Recommended numerical stabilization parameter values

Based on the numerical experiments conducted in this section, we recommend the following stabilization parameters applied in (47) for different physical constitutive material modeling

- Linear elastic model having a Young's modulus E: $C_\kappa = 10^{-5} \cdot E$ and $D_2 = 10^7 \cdot 1/E$.
- Linear elastoplastic model having a terminal yield hardening H: $C_\kappa = 10^{-5} \cdot H$ and $D_2 = 10^7 \cdot 1/H$.

The conducted numerical experiments show that these parameters obtain the highest numerical stabilization of the primal solution during the topology optimization process, while not affecting the physical system behavior for the optimized designs. Applying higher stabilization parameters is possible, but these then significantly affect the physical system behavior for example suppressing physical buckling modes. This might still be reasonable for numerically highly unstable primal solutions for which no solution could be determined otherwise. However, we advise extensive validation of optimized designs achieved by applying higher stabilization factors.

4 | CONCLUSION

We derive very general parameters for a stabilization scheme applying the numerical condition number of the deformation gradient in a hyperelastic constitutive material model demonstrated on both academical and industrial applications. The stabilization scheme is applied successfully to stabilize the primal solutions for a wide range of topology optimization applications. These applications include void elements in both static and quasi-static analyses, yielding void elements in elastoplastic constitutive modeling, homogeneous initial design layouts subjected to highly localized deformations as well as void elements involved in contact during transient dynamic analyses. The number of optimization iterations is drastically reduced compared to previous reported stabilization methods in the literature for geometrically nonlinear topology optimization, since no continuation or projection methods are applied for the material interpolation or filtering. The present approach is independent upon the design variables and only depends on the parameters of the initial constitutive material model applied in the structural modeling. Therefore, the present approach is not limited to topology optimization application and instead is also more generally applicable for stabilizing flexible elements in a geometrically nonlinear finite element analysis.

DATA AVAILABILITY STATEMENT

The data that support the findings of this study are available from the corresponding author upon reasonable request.

ACKNOWLEDGMENT

Open Access funding enabled and organized by Projekt DEAL.

ORCID

Lennart Scherz https://orcid.org/0009-0002-7355-7603
Benedikt Kriegesmann https://orcid.org/0000-0001-5330-9886

REFERENCES

1. Schillinger D, Düster A, Rank E. The hp-d-adaptive finite cell method for geometrically nonlinear problems of solid mechanics. *Int J Numer Methods Eng*. 2012;89(9):1171-1202. doi:10.1002/nme.3289
2. Sigmund O, Maute K. Topology optimization approaches. *Struct Multidiscipl Optim*. 2013;48(6):1031-1055. doi:10.1007/s00158-013-0978-6
3. Bruns T. Zero density lower bounds in topology optimization. *Comput Methods Appl Mech Eng*. 2006;196(1-3):566-578. doi:10.1016/j.cma.2006.06.007
4. Bruns TE, Sigmund O, Tortorelli DA. Numerical methods for the topology optimization of structures that exhibit snap-through. *Int J Numer Methods Eng*. 2002;55(10):1215-1237. doi:10.1002/nme.544
5. Bruns TE, Tortorelli DA. An element removal and reintroduction strategy for the topology optimization of structures and compliant mechanisms. *Int J Numer Methods Eng*. 2003;57(10):1413-1430. doi:10.1002/nme.783
6. Behrou R, Lotfi R, Carstensen JV, Ferrari F, Guest JK. Revisiting element removal for density-based structural topology optimization with reintroduction by Heaviside projection. *Comput Methods Appl Mech Eng*. 2016;380:113799. doi:10.1016/j.cma.2021.113799
7. Wang F, Lazarov BS, Sigmund O, Jensen JS. Interpolation scheme for fictitious domain techniques and topology optimization of finite strain elastic problems. *Comput Methods Appl Mech Eng*. 2014;276:453-472. doi:10.1016/j.cma.2014.03.021
8. Dalklint A, Wallin M, Tortorelli DA. Structural stability and artificial buckling modes in topology optimization. *Struct Multidiscipl Optim*. 2021;64(4):1751-1763. doi:10.1007/s00158-021-03012-z
9. Wallin M, Ivarsson N, Tortorelli D. Stiffness optimization of non-linear elastic structures. *Comput Methods Appl Mech Eng*. 2017;330:292-307. doi:10.1016/j.cma.2017.11.004
10. Bluhm GL, Sigmund O, Poulios K. Internal contact modeling for finite strain topology optimization. *Comput Mech*. 2021;67(4):1099-1114. doi:10.1007/s00466-021-01974-x
11. Buhl T, Pedersen CBW, Sigmund O. Stiffness design of geometrically nonlinear structures using topology optimization. *Struct Multidiscipl Optim*. 2000;19(2):93-104. doi:10.1007/s001580050089
12. Pedersen CBW, Buhl T, Sigmund O. Topology synthesis of large-displacement compliant mechanisms. *Int J Numer Methods Eng*. 2001;50(12):2683-2705. doi:10.1002/nme.148
13. Pedersen CBW, Fleck NA, Ananthasuresh GK. Design of a compliant mechanism to modify an actuator characteristic to deliver a constant output force. *J Mech des*. 2006;128(5):1101-1112. doi:10.1115/1.2218883
14. Lahuerta RD, Simões ET, Campello EMB, Pimenta PM, Silva ECN. Towards the stabilization of the low density elements in topology optimization with large deformation. *Comput Mech*. 2013;52(4):779-797. doi:10.1007/s00466-013-0843-x
15. Ortigosa R, Martínez-Frutos J, Gil AJ, Herrero-Pérez D. A new stabilisation approach for level-set based topology optimisation of hyperelastic materials. *Struct Multidiscipl Optim*. 2019;60(6):2343-2371. doi:10.1007/s00158-019-02324-5
16. Ortigosa R, Ruiz D, Gil A, Donoso A, Bellido J. A stabilisation approach for topology optimisation of hyperelastic structures with the SIMP method. *Comput Methods Appl Mech Eng*. 2020;364:112924. doi:10.1016/j.cma.2020.112924
17. Frederiksen AH, Sigmund O, Poulios K. Topology optimization of self-contacting structures. *Comput Mech*. 2024;73:967-981. doi:10.1007/s00466-023-02396-7
18. Bluhm GL, Sigmund O, Poulios K. Inverse design of mechanical springs with tailored nonlinear elastic response utilizing internal contact. *Int J Non Linear Mech*. 2023;157:104552. doi:10.1016/j.ijnonlinmec.2023.104552
19. Maute K, Schwarz S, Ramm E. Adaptive topology optimization of elastoplastic structures. *Struct Optim*. 1998;15(2):81-91. doi:10.1007/bf01278493

20. Wallin M, Jönsson V, Wingren E. Topology optimization based on finite strain plasticity. *Struct Multidiscipl Optim*. 2016;54(4):783-793. doi:10.1007/s00158-016-1435-0
21. Pedersen CBW. Revisiting topology optimization of continuum structures with elastoplastic response. *15th Nordic Seminar on Computational Mechanics*. Nordica Association of Computational Mechanics; 2002.
22. Kawamoto A. Stabilization of geometrically nonlinear topology optimization by the Levenberg–Marquardt method. *Struct Multidiscipl Optim*. 2008;37(4):429-433. doi:10.1007/s00158-008-0236-5
23. Yoon GH, Kim YY. Element connectivity parameterization for topology optimization of geometrically nonlinear structures. *Int J Solids Struct*. 2005;42(7):1983-2009. doi:10.1016/j.ijsolstr.2004.09.005
24. Yoon GH, Kim YY. Topology optimization of material-nonlinear continuum structures by the element connectivity parameterization. *Int J Numer Methods Eng*. 2007;69(10):2196-2218. doi:10.1002/nme.1843
25. Yoon GH. Topology optimization for nonlinear dynamic problem with multiple materials and material-dependent boundary condition. *Finite Elem Anal Des*. 2011;47(7):753-763. doi:10.1016/j.finel.2011.02.006
26. Kaye A, Stepto RFT, Work WJ, Alemán JV, Malkin AY. Definition of terms relating to the non-ultimate mechanical properties of polymers (recommendations 1998). *Pure Appl Chem*. 1998;70(3):701-754. doi:10.1351/pac199870030701
27. Simulia. *Tosca Structure*. Dassault Systèmes; 2023.
28. Simulia. *Abaqus*. Dassault Systèmes; 2023.
29. Yeoh OH. Some forms of the strain energy function for rubber. *Rubber Chem Technol*. 1993;66:754-771.
30. Sigmund O. On benchmarking and good scientific practise in topology optimization. *Struct Multidiscipl Optim*. 2022;65(11):315. doi:10.1007/s00158-022-03427-2

How to cite this article: Scherz L, Kriegesmann B, Pedersen CBW. A condition number-based numerical stabilization method for geometrically nonlinear topology optimization. *Int J Numer Methods Eng*. 2024;125(23):e7574. doi: 10.1002/nme.7574

APPENDIX A. CONDITION NUMBER-BASED HYPERELASTIC STRAIN ENERGY POTENTIAL PARAMETER COMBINATIONS

TABLE A1 Hyperelastic parameters for the polynomial strain energy potential to yield exponents of up to order 3 of the matrix condition number $\kappa_F(\boldsymbol{F})$ of the deformation gradient $\boldsymbol{F}$ induced by the Frobenius norm $\|\cdot\|_F$.

N	**Parameter**	$(\kappa_F^2(F) - 9)^1 \Rightarrow (\bar{I}_2\bar{I}_2 - 9)^1$	$(\kappa_F^2(F) - 9)^2 \Rightarrow (\bar{I}_1\bar{I}_2 - 9)^2$	$(\kappa_F^2(F) - 9)^3 \Rightarrow (\bar{I}_1\bar{I}_2 - 9)^3$
1	C_{10}	3	0	0
	C_{01}	3	0	0
2	C_{20}	0	9	0
	C_{11}	1	18	0
	C_{02}	0	9	0
3	C_{30}	-	0	27
	C_{21}	-	6	81
	C_{12}	-	6	81
	C_{03}	-	0	27
4	C_{40}	-	0	0
	C_{31}	-	0	27
	C_{22}	-	1	54
	C_{13}	-	0	27
	C_{04}	-	0	0
5	C_{50}	-	-	0
	C_{41}	-	-	0
	C_{32}	-	-	9
	C_{23}	-	-	9
	C_{14}	-	-	0
	C_{05}	-	-	0
6	C_{60}	-	-	0
	C_{51}	-	-	0
	C_{42}	-	-	0
	C_{33}	-	-	1
	C_{24}	-	-	0
	C_{15}	-	-	0
	C_{06}	-	-	0

APPENDIX B. TRACK ROD TECHNICAL DRAWING

Technical drawing for track rod part applied in Section 3.2.4. Note, that the model applied in the optimization is reduced by in-plane symmetry.

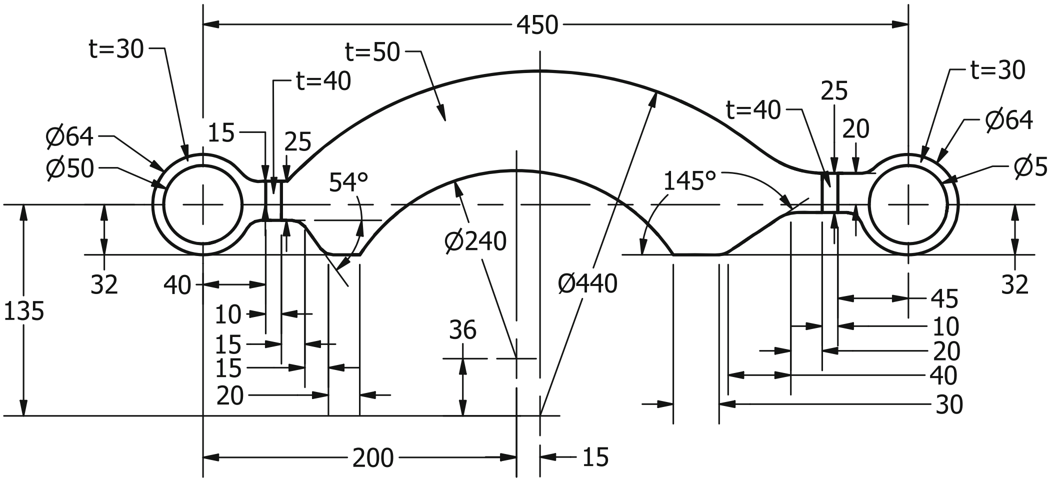

FIGURE B1 Track rod technical drawing in mm.